

High-Fluence Ion Beam Irradiation of Semiconductor Nanowires

Dissertation

zur Erlangung des akademischen Grades
doctor rerum naturalium (Dr. rer. nat.)

vorgelegt dem Rat der Physikalisch-Astronomische Fakultät

von

Andreas Johannes
geboren am 14.03.1986 in Pretoria (RSA)

Gutachter

1. _____

2. _____

3. _____

Tag der Disputation: _____

Contents

1	Introduction	2
2	Background	8
2.1	Ion-solid interactions	8
2.2	Simulation of ion-solid interaction	16
3	Experimental Methods	23
3.1	Nanowire synthesis	23
3.2	Modification	25
3.3	Characterization	28
4	Sputtering of Nanowires	32
4.1	Simulation of the sputter yield	32
4.2	Redeposition	35
4.3	Si nanowire sputtering by Ar ⁺ irradiation	38
4.4	Summarizing discussion	41
5	High Doping Concentrations in Nanowires	43
5.1	Doping and Sputtering	43
5.2	nano-XRF on single nanowires	44
5.3	Pseudo-dynamic simulation	49
5.4	Summarizing Discussion	54
6	Plastic Deformation of Silicon Nanowires	57
6.1	Experimental observation of plastic deformation	57
6.2	Quantification of the Deformation	59
6.3	Knock-on transport of mass	61
6.4	Ion irradiation at large angles of incidence	66
6.5	The proposed deformation mechanism	67
6.6	Summarizing Discussion	75
7	Conclusions and Outlook	77

1 Introduction

Technological progress generally shows a competition between the optimization of the dominating technology and the development of fundamentally new operation principles. An example of this competition is recorded in the “International Technology Roadmap for Semiconductors”, which aims to guide the scaling of digital devices to follow “Moore’s Law” of improved performance, and the white paper “Towards a ‘More-than-Moor’ roadmap”, which examines opportunities to include non-digital functionality where performance does not necessarily have to scale with size. Both are available at the ITRS website [map15]. A shift in operating principle is found, for example, in data storage, which changed fundamentally when the effect of giant magneto-resistance (GMR) was discovered in 1988 [BBF⁺88, BGSZ89]. This quickly formed the basis for the standard hard-drives (HDD) and HDDs soon dominated PC data storage. Nowadays, the older principle of flash memory is making a comeback in solid state drives (SSD), which begin to replace HDDs. They owe their viability (cost, speed and storage density) almost entirely to the advanced miniaturization, allowing the production of a floating gate for a transistor on a scale down to tens of nanometers per single *bit*, while producing *billions* of *bits/cm²* [MME13]. This shows, that it is not *a priori* possible to discern with certainty which approach is going to produce the best results, so that much room is left for open minded fundamental research in general and on semiconductors in particular.

In the wake of the miniaturization aimed at the improvement of IT hardware technology, the new, multi-disciplinary field of nanotechnology has emerged. The scope of the field is illustrated by the high number of journals dedicated to research at the nanoscale. This includes semiconductor science, but in the leading journals *ACS Nano* [?], *Advanced Materials* [Adv15b], *Advanced*

Functional Materials [Adv15a], *Nano Letters* [Nan15a], *Nature Nanotechnology* [Nat15], *Nano Today* [Nan15b], *Nanotoxicology* [Nan15c], *Small* [Sma15] and others, fundamental research and applications of nanoscale devices and effects from all natural sciences are published.

The specific class of nanomaterials investigated within this thesis are semiconductor nanowires, which have gained a significant amount of interest [HMF⁺01, CWPL01, DHC⁺01, XYS⁺03, LW07]. ‘Nanowire’ is a term used for many morphologies, but it seems a reasonable name for structures with a cross-section that is between 1×1 and $1000 \times 1000\text{ nm}^2$ and a large length to form a high aspect ratio. One of the general aspects of this shape and also of nanostructured materials in general, is that the surface properties play a dominating role. This is simply caused by the large surface-to-volume ratio. Because this ratio in general is proportional to $1/r$ for a body with a characteristic constraining length of r , it becomes very large for small structure sizes. The wire shape has an inherent advantage over three dimensionally constrained particles (nanoclusters, quantum dots etc.), in that it is easier to define contacts and drive a current through a nanoscale wire than through a nanoscale dot.

The high surface to volume ration ensures that a semiconductor nanowire with two contacts at either end is already a very sensitive device. Such simple devices have been shown to be possible gas-sensors [SCRZ09], they could measure the *pH* inside a cell [CWPL01] or the impact of a single ion [JNGR11]. By functionalization of the surface, it is, as one example of many, possible to create a selective biological sensor that can even detect the attachment of a single viruses [PZH⁺04]. Additional functionality can be gained by adding impurities to semiconductor nanowires, because this dramatically changes their electronic properties [SN06]. For example, changing the doping from *n* to *p*-type within a nanowire creates a *pn*-junction that can be used as a solar cell [KTK⁺08, CZP⁺12], while the combination of *n* and *p*-type nanowires can be used to fabricate a thermo-electric generator [Sch14].

A particularly flexible method to add impurities to semiconductors is ion beam irradiation, because it can be used to ‘mix’ (i.e. dope) virtually any target material with a precisely controlled number of atoms of practically any

1 Introduction

element. Ion beam doping is a well established technology, and it was and is a key part in the processing and development of semiconductor technologies [HH12]. In general, ion beam doping has the advantage over doping during the synthesis of nanostructures, because it is not inherently limited by the chemical potentials and thermodynamics, which typically have to be carefully controlled for the synthesis of nanostructures. It is a non-equilibrium physical process by which different elements can forcefully be introduced into a target matrix with much higher energies than those involved in chemical bonding. The extent of disorder created in the target during this bombardment, whether the intermixing is thermodynamically stable and whether a desired (crystalline) order can be reestablished by thermal annealing is in the focus of ion-beam physics. A good background on this can be gained from dedicated literature [ZLB85, Eck91, Nas08, Sch12].

Typical ion ranges for the doping of semiconductors lie in the range of 10-100 nm. Therefore, ion beam irradiation of nanostructures of the same dimension will show some interplay between the irradiated structures' dimensions and the ion range. The many practical applications of the combination of ion beams and nanostructures warrants general investigations of the nanostructure - ion beam interaction and the topic has therefore gained increased interest very recently [Bor12, GHB⁺13, NSUM14, JHMR15, UBNM15].

A specific example in which the combination of nanostructures and ion beams is advantageous is the ion irradiation of diamond to create nitrogen-vacancy clusters [BHK⁺10]. The diamond is nanostructured to facilitate efficient extraction of light, while ion irradiation with nitrogen creates nitrogen-vacancy clusters very effectively. These are promising components in a future quantum information device. The precisely controlled ion irradiation, makes it possible to implant a well defined number of ions with reasonable spacial accuracy. This control is extravagantly demonstrated by the possibility of single ion irradiation [MVB⁺06, Ohd08].

In addition to this extremely low ion fluence example of ion irradiation, the next two examples of the concurrence of nanotechnology and ion-irradiation led more or less directly into the fundamental investigations of high fluence irradiation presented in this dissertation. Firstly, there is the search for a

nanostructured diluted magnetic semiconductor for which *Mn* doped *GaAs*-nanowires are a good candidate. Because *GaAs* nanowires typically grow above 450°C but *MnAs* segregates from $Ga_{(1-x)}Mn_xAs$ at around 350°C [DO06, SSK⁺11], there is no straightforward way to dope *GaAs*-nanowires with high concentrations of *Mn* during their growth. However, it can be achieved by implanting *Mn* in *GaAs*-nanowires. Best results are achieved when the irradiation is performed at elevated temperatures, hot enough to minimize disorder introduced by the ion beam, but cold enough to prevent segregation of *MnAs* [BMB⁺11, PKB⁺12, Bor12, KPJ⁺13, PKJ⁺14].

Conversely, the “wiring quantum dots” project, through which this thesis was funded, aimed to utilize the segregation of ion-implanted material in a nanowire to form nanowires decorated with nanoclusters. When *Si* nanowires are irradiated with high fluences of *In*⁺ and *As*⁺ and subsequently annealed with a flash-lamp, separated *InAs* slices form within the *Si* nanowires [PGL⁺14, Gla15]. The supersaturation of *Si* with *In* and *As* by ion implantation can thus be utilized to create *Si-InAs* nanowire hetero-structures from a *Si* nanowire template in a relatively straightforward manner.

A further important example of the intersection of nanotechnology and ion beams is found in the ubiquitous focused ion beam (FIB) systems. The production and development of many of the novel nanoscale devices on the horizon often requires the precise ion beam milling that FIBs provide with a resolution of few nanometers [KFM⁺01, GTC⁺10, CCJ⁺13]. In all the examples given so far, and virtually per definition in the last one, the typical structure sizes irradiated are in the same order of magnitude at the range of the impinging ions. Understanding how this affects the ion-matter interaction can be crucial to the successful outcome of the respective experiments.

In the effort to understand principles and fundamental interactions on the nanometer length scales, nanowires are a very good model system to investigate, because their geometry is fully characterized by their height and radius. Spheres, which would have a degree of freedom less, are more difficult to handle, because the unavoidable proximity of a substrate may influence their behavior [HCA02, KZB⁺09, Mö14, JHMR15]. The understanding of the ion-nanostructure interaction gained by investigating irradiated nanowires is prin-

1 Introduction

cipally transferable to any nanostructure. However, this can hardly be done in a general way explicitly, because the possible shapes of nanostructures are uncountable.

This dissertation will begin with an overview of the ion-solid interaction focused on the accuracy of simulations of this interaction. A detailed review of effects and literature relevant to the ion irradiation of nanostructured materials is also given (Chapter 2.1). Next, the methods used for the experiments are briefly outlined (Chapter 3). This dissertation adds to the growing field of nanostructure - ion beam interaction by discussing three effects which are especially important in high ion fluence irradiation. A separate chapter is dedicated to each high ion fluence experiment.

Chapter 4 - Sputtering of Nanowires

In the dissertation of Dr. C. Borschel [Bor12] the program *iradina* [BR11] was developed and used to simulate the ion irradiation of nanostructures. It predicts an enhanced, diameter-dependent sputter yield in nanostructures. Chapter 4 discusses the simulation and compares its predictions with experimentally obtained diameter-dependent sputtering in nanowires. Some first results on the sputtering during *Mn* irradiation of *GaAs*-nanowires are published elsewhere [JNP⁺14]. The results presented here are on *Ar* irradiated *Si*-nanowires. They were obtained in close cooperation with Stefan Noack [Noa14] in his M.Sc. and also published in reference [JNW⁺15].

Chapter 5 - High Doping Concentrations in Nanowires

The concentration of dopants does not follow a linear increase with the fluence of ions implanted for high fluences. It has already been observed that sputtering of the target will dynamically change its composition during the ion irradiation in addition to the intended change by incorporation of the ions within the target material [ME84, MEB88, MIS⁺91, SO93, Eck00]. This effect is enhanced in nanostructures, first, because the sputtering is enhanced when compared to bulk samples, as demonstrated in Chapter 4, but also because there is simply less material. Hence, the effect of removing material by sputtering already

becomes significant at lower fluencies in nanostructures than in bulk. The presented results were acquired by compositional analysis using nano-XRF performed on 175 keV Mn⁺ ion irradiated ZnO nanowires and are partially published in reference [JNP⁺14]. They are discussed in comparison to a pseudo-dynamic simulation performed using results from *iradina*.

Chapter 6 - Plastic Flow in Silicon Nanowires

In high ion fluence irradiated *Si* nanowires an unexpected tendency of the nanowires to become shorter was observed. Chapter 6 presents a dedicated investigation into this plastic deformation of *Si* under ion irradiation which has been previously seen only in high energy ($\geq MeV$) ion irradiations [Vol91, TR95, HKW04, HKW05]. These results were also obtained in part within the M.Sc of Stefan Noack [Noa14] and are published in reference [JNW⁺15]. A probable mechanism for the deformation can be presented by comparing the experimentally observed deformation with dedicated *iradina* simulations and literature on MD simulations of similar conditions.

2 Background

2.1 Ion-solid interactions

Electronic Energy loss

An energetic ion impinging on a solid will lose its kinetic energy E to the solid over the distance traveled x in a variety of processes. The electronic stopping power S_e is well described for a large energy range by the Bethe (sometimes “Bethe-Bloch”) formula [Bet30, Blo33] derived using the Born approximation perturbation theory on the impact between the ‘fast’ ion and the ‘slow’ electrons in the solid:

$$S = \frac{dE}{dx} = -A \cdot \frac{\rho Z_2 \cdot Z_1^2}{\beta^2} \cdot \left[\ln\left(\frac{B \cdot \beta^2}{Z_2 \cdot (1 - \beta^2)}\right) - \beta^2 \right], \quad (2.1)$$

with A and B positive combinations of constants, ρ the density and Z_2 the atomic number of the target, Z_1 and $\beta = v/c$ the atomic number and relativistic velocity of the ion. Corrections to this formula are especially necessary for low ion energies, but in detail they are dependent on the target composition, the ion energy and ion mass in a non-trivial way. Figure 2.1 illustrates stopping regimes and where corrections are required to the Bethe formula. The Figure and discussion are adapted from reference [Sig04].

At high ion energies ($> 1 \text{ GeV/amu}$, labeled “Relativist.”) highly relativistic effects have to be taken into account. At these energies we have, for example, the generation of Cherenkov radiation. The horizontal line labeled “Shell corr.” marks the Thomas-Fermi velocity ($Z_2^{2/3} v_0$) of the target electrons, with the Bohr velocity $v_0 = e^2/\hbar = 25 \text{ keV/amu}$. In the parameter-space below this line the ion is moving at speeds comparable to that of electrons in the target, so that a correction for the energy levels (shells) in the target has to

2.1 Ion-solid interactions

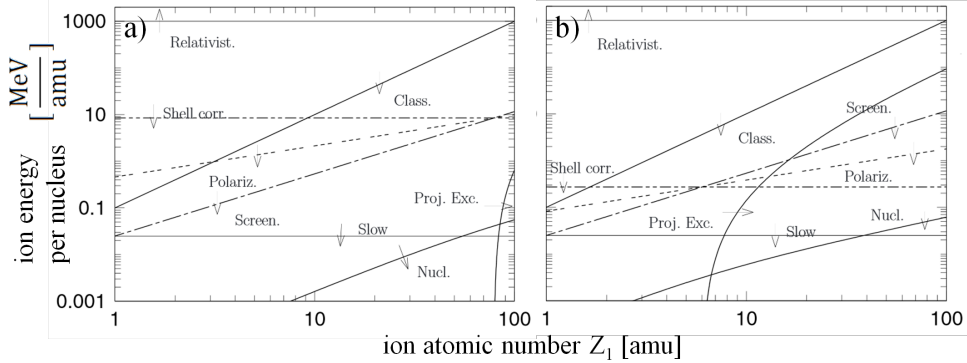


Figure 2.1: Illustration of the dominant effects on the electronic stopping power for an ion of mass Z_1 and energy E in Au a) and C b). Adapted from [Sig04].

be made. In the low energy area below the second horizontal line labeled “Slow” (at $25 \text{ keV}/\text{amu}$) the ion is traveling at speeds below the Bohr velocity of the target electrons. Here, the ion velocity is only comparable to that of the valence electrons in the solid. Now the actual electron density distribution and chemical nature of the solid becomes relevant, which is of course not considered in the general Bethe formula. Therefore, for low ion energies a general and accurate theoretical prediction of the stopping power becomes impossible. Specific ion-target combinations require dedicated investigations.

Above the line showing the Thomas-Fermi velocity of the ion ($v = Z_1^{2/3}v_0$, “Screen.”) the ion can be assumed to be stripped of all its electrons. Below, an additional screening function must consider the effective charge of the ion, the theoretical framework for the correction is found in the Lindhard theory [Lin54]. Below the curve labeled “Proj. Ext.” the ion (projectile) carries a comparable number of electrons to the target making excitation processes in the electronic configuration of the ion significant.

For ion velocities $v < (Z_1 Z_2)^{1/3} v_0$ (labeled “Polariz.”) a higher order (Z_1^3) correction term to the Bethe formula becomes relevant due to the Barkas-Andersen effect. Barkas et al. found that the stopping power was unequal for particles and anti-particles [SBB53]. This leads to a charge-dependent correction term quantified by Andersen et al. [ASS69, SS14]. Below the

2 Background

line marked “Class.” ($Z_1^2 \cdot 100 \text{ keV/amu}$) classical Bohr orbits can be used for electrons around the ion, this is a *sufficient* criterion for the derivation of the Bethe formula not a *necessary* one.

Thus, electronic stopping S_e is the sum of the interactions between the ion and the electrons in the irradiated solid. In the simplest case a target atom is ionized, followed by a host of effects such as characteristic X-ray emission and Auger electron emission associated with the relaxation of this excited state. Analogously, excitation in a semiconductor is associated with band to band transitions, exciton recombination etc. [Wie88, BFS⁺¹²]. The luminescent and fluorescent relaxation mechanisms are, however, generally not very efficient. Most of the energy deposited in the electronic system will be turned into kinetic energy of electrons and subsequently converted to phonons/heat. This happens very locally on the nm scale of the electrons mean free path and thus also very quickly, within the order of ps [TDP92, Nas08].

The effects of such local heating on a solid are diverse. Defects and amorphous regions may either appear or disappear, depending on the material and its history. For large ion masses and energies (swift, heavy ions), the deposited energy density becomes large enough to form an “ion track” around the path of the ion. Swift heavy ion tracks are a whole field of research outlined well by references [TDP92, MK97, WKW04]. Very large electronic losses have to be treated carefully, because a large percentage of the electrons within the track are energized and some electrons also gain a significant amount of kinetic energy.

The energies used in this dissertation are in the order of $\approx 100 \text{ keV}$ with elements of mass $\approx 100 \text{ amu}$. The energy regime investigated in this dissertation is thus right at the bottom of the area plotted in Figure 2.1. Electronic stopping is not dominant, so that it is sufficient to treat the electronic energy loss as a local heat source.

Nuclear energy loss

In the region marked “Nucl.” in Figure 2.1, at low ion energies and for heavy ions, the interaction with the electronic system becomes weak. Here, the con-

2.1 Ion-solid interactions

tribution of the coulomb interaction between ion and individual target atoms as a whole become the main contribution to slowing down the ion. This is called nuclear stopping in contrast to the electronic stopping discussed in the previous section, because kinetic energy is transferred to the target nuclei, not just the electrons. Its first observation was in the famous Rutherford (Geiger–Marsden) experiment [Rut11], which was groundbreaking to the understanding of the structure of matter. Nuclear energy loss arises from the kinetic energy, which is transferred from the energetic ion onto an atom in the target. Because the impinging ion can transfer considerable energy to an atom, the atom can leave its lattice site and in turn collide with other atoms in the target, leading to the formation of a collision cascade. This displacement of atoms from their lattice position is the main contribution to irradiation damage and sputtering of the target.

The amorphization of crystalline semiconductors has been investigated extensively, a good review is given by reference [WWS12]. The damage production depends strongly on the properties of the irradiated semiconductor and on the density of the collision cascade caused by the irradiating ion. In general, the defects produced by nuclear energy loss are Frenkel pairs. On further irradiation, interstitials and/or vacancies can agglomerate to form extended defect clusters, which initiate amorphization. The ion fluence at which the material is amorphized is highly temperature dependent, because Frenkel pairs can anneal at elevated implantation temperatures. This can lead to an arbitrarily high amorphization fluence, if the annealing of defects is faster than their creation. A typical ‘radiation hard’ material is ZnO , which is not amorphous even after 10^{17} cm^{-2} of 200 keV Ar^+ irradiation at 15 K [WWS12]. An arbitrarily large amorphization threshold can also be obtained for Si irradiated with 300 keV Ar^+ at $300^\circ C (\approx 600 \text{ K})$ [PMB04].

In addition to the activation of defect recombination by increasing the ‘global’ temperature, an increased local temperature by the energy deposited by the ion will also lead to ‘dynamic annealing’ [Dha07]. The reduction of structure sizes leads to larger dynamic annealing, because there is less material into which the energy deposited by the ion can dissipate, leading to higher local temperatures. This was shown in the Mn irradiation of $GaAs$

2 Background

nanowires [Bor12, JHMR15] and was used to improve the magnetic properties of the *GaAs:Mn* nanowires [BMB⁺11, PKB⁺12, KPJ⁺13, PKJ⁺14].

The binary collision approximation

A typical assumption in the theoretical treatment of nuclear energy loss is the binary collision approximation (BCA) for the ion and the target atoms [Eck91]. Under this assumption nuclear stopping is treated as a series of collisions between single particles. With the additional assumptions of 1) a spherically symmetric interaction potential and 2) the neglect of possible electronic effects (chemical binding) between the collision partners, the angular-momentum is conserved in the collision and the classical scattering-integrals can be solved [ZLB85].

As an example, the resulting trajectories of a *Si-Si* collision at 10 eV is plotted in Figure 2.2. The large difference between the Moli  re screened Coulomb potential [Mol47] and the “*Si-Si*” potential [HFH⁺90], derived by Dirac-Fock-Slater calculations, is clearly visible. The former is a purely repulsive Coulomb interaction, while the latter includes an attractive interaction for large interatomic distances similar to the well known Lennard-Jones potential [Jon24, Eck91]. For high energy collisions a “universal” Ziegler-Biersack-Littmark (ZBL) potential based on a screened Coulomb interaction is quite successful [ZLB85], however for low energy collisions a generalized formula cannot be accurate and specific potentials have to be developed for each combination of collision partners [Ded95, NRS97, ANNK02, ND08].

In addition to this problem of finding the correct interaction potential for a collision, depending on the ion and the atomic structure of the irradiated material, the collision parameters relevant to low energy collisions are within the order of the inter-atomic distance of a few Å, as shown in Figure 2.2. The assumption that this is still a binary collisions can no longer be valid. In conclusion, it has to be noted that similar to the electronic stopping case, the assumptions for a generalized treatment of nuclear stopping are well fulfilled for large ion energies, but lose their validity at low energies $\ll 1 \text{ keV}$.

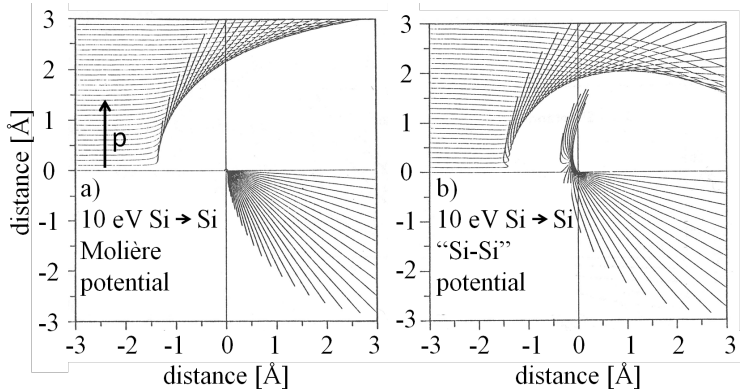


Figure 2.2: Trajectories of a 10 eV $Si-Si$ collision for a) Moli  re and b) “ $Si-Si$ ” potential. The trajectories end after the same elapsed time for each impact parameter p . Adapted from [Eck91].

Sigmund theory of sputtering

A prominent role in this dissertation will be played by a special effect of nuclear energy loss arising when the path of a recoiled atom intersects the targets surface: sputtering. The foundation of a sputter theory was laid by Sigmund [Sig69]. The nuclear stopping of ions leads to the formation of highly branched collision cascades and most of the recoiled atoms are found at the end of the many branches. Because of this, the majority of sputtered particles has a low energy and thus a low range in the material [Tho68]. Therefore, predominantly atoms close to the surface of the target contribute to the sputter yield. The number of atoms sputtered per impinging ion can be estimated by calculating the nuclear energy loss at the surface of the irradiated material, divided by a factor to account for the probability of an atom leaving the solid. The probability for the atom to leave the solid includes geometric considerations and the ‘surface binding energy’ (SBE). A possible model for an atom leaving a solid is that of a potential plateau with the height of the enthalpy of sublimation, which has to be overcome by the atom approaching the surface. This equates the energy required for sputtering an atom to the thermal energy required for sublimation. For metals this is a good assumption, because the metallic bond is undirected and mediated by the electron

2 Background

gas. However, the SBE model for sputtering neglects all effects related to the directionality of the local binding forces experienced by the atom to be sputtered and the modification of the surface by repeated removal of atoms, which will be relevant in compounds with covalent or ionic bonds.

A reasonable assumption for the mean nuclear energy deposition distribution is a Gaussian ellipsoid, with the center at the ion range and the longitudinal and lateral straggling naturally defining its extensions. This approach was used by Sigmund to arrive at a good explanation for the energy dependence of sputtering from flat surfaces [Sig69]. Starting at low ion energies, the sputter yield will initially increase with increasing energy, simply due to more energy being available. For further increasing ion energy, however, the ion range becomes larger, leading to a predominant deposition of the energy deeper inside the target, away from the surface. A maximum is thus found at ion energies where the ion range is in the order of the longitudinal straggling. The angle dependence of sputtering can also be explained by the increased deposition of energy near the surface for larger angles of incidence, as shown in Figure 2.3.

With the situation illustrated in Figure 2.3, the Sigmund theory can explain surface roughening by ion bombardment. For example, the Bradley-Harper theory of ripple formation on ion irradiated planes relies on the anisotropic sputtering predicted by the Sigmund model applied to a structured surface [Sig73, BH88]. The increased sputtering at a point (C), downstream from the point where the ion enters the target (O), leads to an enhancement of surface roughness.

The Sigmund theory can also be applied to curved surfaces. For nano-sized spheres or cylinders, the Sigmund theory can be invoked to predict that the sputter yield will be maximum when the ion range is comparable to the nano-structure diameter. Consider sputtering for a fixed ion energy and a varying diameter, illustrated in Figure 2.4. At extremely large diameters atoms can only be sputtered from the flat surface (A in Figure 2.4) facing the ion beam. The sputter yield will still be larger than for an unstructured bulk sample, because the local angle of irradiation is increased for non central impacts. For decreasing diameters the curvature of the nanostructure increases, further in-

2.1 Ion-solid interactions

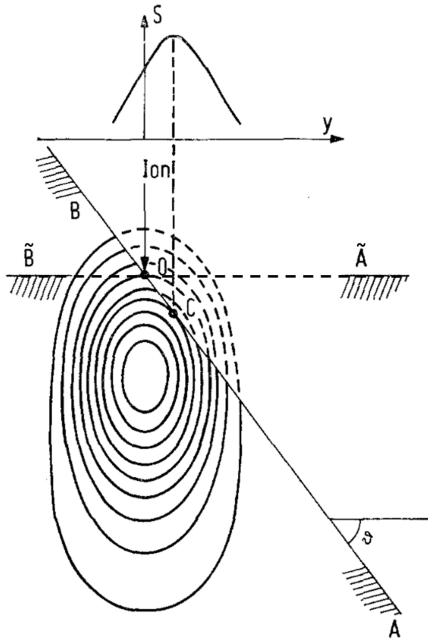


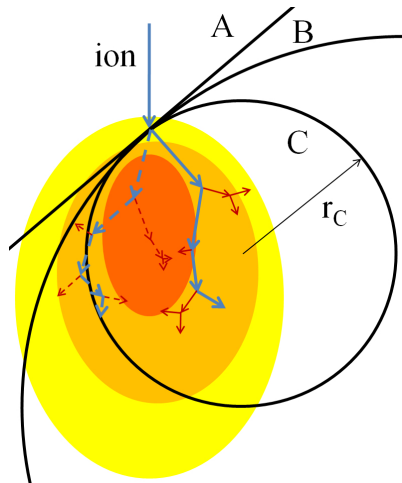
Figure 2.3: Illustration of the Sigmund model of sputtering for irradiation of a bulk sample at an angle θ . The ion enters the target at the point O and deposits energy by nuclear stopping as indicated by the oval contours. The energy deposited along the inclined surface BA is larger than that for the perpendicular surface $\tilde{B}\tilde{A}$ leading to increased sputtering for irradiation at an angle. Also the deposited energy and thus sputtering is not largest exactly at the point of incidence O, but further down at the point C. This is illustrated by the projection of the sputter yield ‘S’ onto the lateral dimension ‘y’. Adapted from [Sig73].

creasing the intersection area between the estimated energy distribution and the nanostructure (B in Figure 2.4). Once the diameter is in the order of the ion range, ‘forward’ sputtering along the direction of the ions initial path becomes possible (C in Figure 2.4). There is a maximum sputter yield for a radius comparable to the ion range, because the total surface area shrinks as $1/r^2$, reducing the sputter yield again for decreasing diameters.

This model is obviously limited, because the energy distribution is assumed to remain constant even if it is intersected by the target surface (dashed lines in Figure 2.3). The maximum in the Gaussian ellipsoid approximation of the mean energy deposition is found where many of the branches of collision cascades overlap. A constant distribution wrongly includes those ion paths that would have left the nanostructure, as shown by the dashed ion trajectory in Figure 2.4. Thus, a more detailed description of the process is required.

2 Background

Figure 2.4: Illustration of the Sigmund model of sputtering for irradiation of a curved surface. For an infinite curvature radius (straight line A) a non-central impact is the same as irradiation at an angle, as shown in Figure 2.3. For decreasing radii (B) the intersection between the colored energy distribution and the surface is increased. For small radii (r_C , C) forward sputtering appears. Two exemplary ion paths contributing to the colored average energy distribution are shown. The dashed path leaves and returns to the the smallest structure C.



2.2 Simulation of ion-solid interaction

In practice, the theory of ion-solid interactions is implemented in simulation tools, which allow the experimenter to predict experimental outcomes. Most frequently the energy dependence of the ion range is obtained by such simulations and used to decide which ion energy and ion fluence of irradiation is needed to create a desired doping concentration profile. On a more fundamental level, an experimentally observed behavior can be understood better by comparing it to various simulations to discern the dominating effects. The two main simulation approaches used for the ion-solid interactions are Monte-Carlo (MC) and molecular dynamic simulations (MD), both outlined in the following sections. Two dated, but highly recommendable reviews on the topic are given in references [And86, Eck91].

Monte-Carlo simulations

Monte-Carlo codes are simulation codes that use random numbers for simulations. After numerous simulations with different randomized outcomes, a statistical approximation of the likely outcome can be derived. With the BCA, the solid ion-interaction lends itself very well to MC simulation, because the

2.2 Simulation of ion-solid interaction

evolution of a collision cascade can be simulated by following the paths of the ion and all recoils reiteratively from one collision event to the next. The probability of a collision can be determined from the cross-sections determined by the interaction potential between the projectile and the atoms in the target. According to this probability, a randomized distance traveled in a straight line by the projectile is determined. The particle's kinetic energy is reduced by the electronic energy loss accordingly. This has the underlying assumption of a ‘random material’ and crystal structure effects such as channeling are not reproduced by such a simulation. Two further random numbers are used to determine the impact parameter and azimuthal angle. The trajectories of the projectile and target atom in the plane of impact after the impact are determined by this impact parameter, the interaction potential and the particle energy, as shown in Figure 2.2.

Examples of simulation codes implementing this approach in planar targets are TRIDYN [ME84], SDTrimSP [BMS⁺08], cordeo [Sch08], COSIPO [Hau84] and, by far the most popular, SRIM [Zie12]. The target composition is treated dynamically in TRIDYN and SDTrimSP, changing with the incorporation of ions and with selective sputtering of target atoms and the incorporated ions. It is clear from the discussion of Chapter 2.1 and Figure 2.4 that the irradiation of a nanostructure can not be approximated well with a planar simulation. Therefore, the recently developed TRI3DYN [Mö14] and *iradina* [BR11] run a BCA MC simulation in a volume subdivided into rectangular voxels containing either vacuum or material to represent a three dimensional, structured target. TRI3DYN even includes dynamic composition and structural relaxation during the irradiation on a three dimensional simulation volume, but unfortunately it is not publicly available yet. Several *iradina* simulation results will be discussed in this thesis, so some points on the expected accuracy have to be made.

The advantage of MC BCA simulations in general is that the direct simulation of the ion trajectories gives an accurate prediction of the final distribution of the ions in the target. This is a result of the sufficient accuracy of the previously discussed underlying theory of the energy losses for high ion energies. These predominantly determine the distance traveled by the ion in a colli-

2 Background

sion cascade and also the distribution of nuclear and electronic energy loss. Because the simulation directly follows the ions path, this accuracy can be expected to be upheld in the irradiation of nanostructures, such as nanowires. The concentration of incorporated ions is somewhat lower in nanowires than in bulk targets, because there are more possible paths that lead to the ions being scattered out of the nanowire, than there are in the irradiation of a bulk surface, see Chapter 2.1, Figure 2.4 and reference [Bor12].

Predicting the damage caused in the material by nuclear energy loss is a much more difficult prospect. The *iradina* code checks at each collision whether the target atom acquires more energy than the “displacement energy”, which is a material specific parameter. If an atom has less than the displacement energy after a collision, it is assumed to remain bound in its place and the energy is converted into phonons. Atoms with more energy are displaced, creating a Frenkel pair, which is counted as an interstitial at the location where the atom finally comes to rest and a vacancy at its point of origin. The displacement energy is experimentally accessible for crystalline materials by electron irradiation experiments in which the irradiating electron energy is in the order of MeV [CW65]. From the electrons’ impulse and mass the maximum transferred energy can be calculated. The defects produced as a function of electron energy can thus be used to determine a threshold energy transfer for the creation of point defects, and this value is defined as the displacement energy. This is not possible for amorphous materials, where point defects are ill-defined. Also, the number of Frenkel pairs is only an estimation at the *creation rate* of the defects. The critical role that defect mobility, agglomeration and annealing plays in ion irradiation, especially at elevated temperatures, is totally neglected [PMB04, Nor14].

Better results can be expected for the computation of sputtering by MC simulation tools, for which an excellent review is given in reference [Bie87]. The difficulty is that for low projectile energies the interaction with both the nuclear and the electronic system are not generalizable, as discussed in Chapter 2.1. This is a problem, because the dominating contribution to sputtering is made by low energy recoils [Tho68]. The various relevant interaction potentials, however, differ most at low energies. In addition, the SBE model used

2.2 Simulation of ion-solid interaction

for Sigmund sputtering is just an approximation of the complexities arising at real surfaces. For metals the situation is most favorable and in reference [Bie87] sputter yields of various metals are reproduced quantitatively. More recently, in reference [HZM14] by Hofsäss et al., good results on the sputtering of *Si* and *Ge* were obtained using the *Kr-C* [WLB77] potential, which was found to be superior to the ZBL potential [ZLB85]. In *iradina* only the ZBL potential is implemented, however, neither the *Kr-C* nor the ZBL potential reproduce the angle-dependent potential of covalently bonded solids such as *Si* [SW85, Ter88]. Radially symmetric potentials are always only an approximation and which potential provides the better approximation in which scenario is not generally clear.

Hofsäss et al. [HZM14] also report a change in the dependence of sputtering on the angle of incidence for different interaction potentials. This might be worrisome even for the qualitative dependencies in the irradiation of nanostructures investigated in this thesis. However, the effect of different potentials on angle-dependent sputtering is caused by the change in the critical angle for scattering at the surface of the impinging ion, not by a later change in the distribution of the nuclear energy deposition within the target [EHHF92]. Because the critical grazing incidence angle is close to 0° regardless of the interaction potential for the relatively high energies ($\approx 100\text{ keV}$) used in this dissertation [YS84], the accuracy of qualitative predictions will be unaffected. Finally, Hofsäss et al. [HZM14] also compared reported experiments on the compounds *Ta₂O₅* and *SiO₂* with simulations, finding that composition changes, caused by preferential sputtering of one element in the compound, play a significant role. This makes dynamic simulations necessary. Because this is not possible in *iradina*, it will be discussed where relevant.

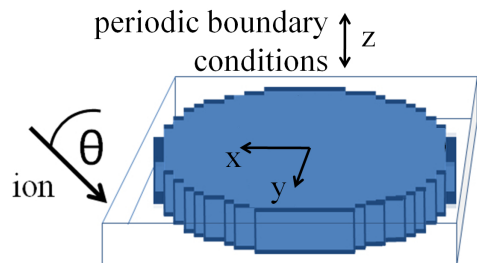
Even though *iradina* can implement an analytical description of a cylinder [Bor12], most of the simulations in this work were performed on the voxel based simulation volume, because this granted more freedom in the creation of the simulation volumes. A typical simulation volume is shown in Figure 2.5. The number of target atoms leaving the simulation volume per impinging ion gives the sputter yield. To ensure *iradina* accounts for the surface binding energy correctly, the outermost voxel of the simulation volume has to contain

2 Background

vacuum, so that a sputtered atom makes a material-to-vacuum transition inside the simulation volume. Where the axial distribution was not relevant, the voxel z -size was set to 10 nm with periodic boundary conditions. The accuracy of the approximation of a curved surface in the xy direction, such as the surface of the cylindrical nanowires, is obviously dependent on the voxel size. Because the surface of the approximation by rectangular voxels of a cylinder is strictly larger than the analytical surface, sputtering may be slightly increased. Also, the possible ions' impact angles are limited to the angle between the ion beam and the plane surfaces of the voxels facing the ion beam, so that the impinging angle is always larger in the voxelated surface than for the analytical surface. However, this will have no large effect, because, as before, the small critical angles for reflection of ions are restricted to the very outermost edges of the nanowire. Considering these effects, it was found that for voxel edges of 2 nm and below only a negligible influence of the voxel size on the sputtering remained.

Figure 2.5: *add image with voxels*

Typical implementation of a nanowire for an *iradina* simulation. The ions enter the simulation volume at $x = 0$; $y, z = \text{random}$ with an angle to the z -axis of $\theta = 45^\circ$. The x and y direction have 102 voxels of $0.02 - 2\text{ nm}$ edge-length so that nanowire with diameters of $2 - 200\text{ nm}$ can be simulated. The z -direction is periodically continued.



In summary, the prediction of sputtering, as simulated by *iradina* in this thesis, is expected to be dependable with respect to the qualitative relationship between ion range and structure size, and sputtering. Quantitative sputter yields will, however, be inaccurate.

2.2 *Simulation of ion-solid interaction*

Molecular dynamic simulations

The MC BCA simulations outlined so far inherently neglect all effects occurring when more than two particles move at the same time. Molecular dynamic (MD) simulations, however, follow the path of every particle in the simulation volume individually, calculating the interaction potential between them at every time step [AW59]. Obviously this is much more computationally expensive than the BCA and simulation volumes and times are thus limited. Nevertheless, the method can be applied to ion irradiation [Nor95] and increasing computer power has led to the simulation of ever higher particle energies, which require a larger simulation volume and time [GHB⁺13, BD14, ABU15]. The interactions between the target atoms in the MD simulations have to recreate the atomic structure, thermal vibrations etc., so that the low energy regime of the interaction potential is critical and has to be adapted to the specific problem [Ded95, NRS97, ANNK02, ND08, Pri12, PGB13]. Electronic energy loss can be included as a frictional force, however, treating this energy in a consistent manner is a problem, because the electronic system is typically not explicitly represented. Since MD simulations can reproduce the thermal evolution of a system, references to relevant MD simulation studies will be included in the discussion of results in this thesis.

Relevant simulations in literature

Two recent investigations on sputtering of spherical [NSUM14] and cylindrical [UBNM15] nanostructures have to be mentioned here, because they overlap significantly with the studies made in this thesis. These publications have found the Sigmund model, as it was discussed in Chapter 2.1, to be a decent first approximation for sputtering of nanostructures. They go on to compare the sputter yield results from MC and MD simulations and discuss its diameter dependence. Unfortunately, the nanowire diameters investigated by MD are quite small owing to the computational costs. They find that for decreasing nanostructure diameters sputtering of clusters and thermal evaporation become increasingly important due to the lower number of atoms amongst which the ion deposited energy is distributed. This dissertation adds to results

2 Background

of these studies with explicit simulations of diameter and energy-dependent sputtering of nanowires in Chapter 4.1 and an experimental investigation of this dependency in the following Chapter 4.3.

3 Experimental Methods

3.1 Nanowire synthesis

Nanowire synthesis can be categorized according to two approaches: “bottom-up” and “top-down”. The “bottom-up” approach relies on the self-organized arrangement of matter using an inherent anisotropy in the growth mechanism to create nanoscale structures. Depending on the material, crystal quality, morphology, infrastructural requirements, the quantity to be produced etc. there is a large variety of processes available for synthesis. The *ZnO* [BMS⁺06, Sti08, Mü09, CZC⁺10, Ogr13] and *Si* [LSH⁺08] nanowires investigated in this dissertation were grown using vapor transport, pulsed laser deposition (PLD) and chemical vapor deposition (CVD) respectively.

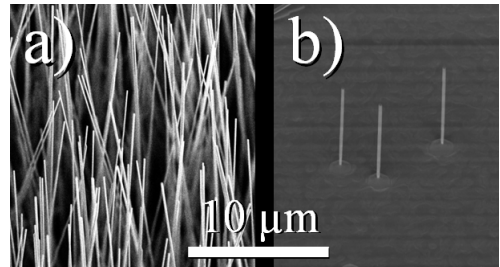
A very common mechanism to create the anisotropy required to get the one dimensional growth of nanowires is the vapor-liquid-solid growth (VLS) first described by Wagner and Ellis [WE64]. The growth of the “bottom-up” nanowires used in this thesis relies on the VLS mechanism. The variety of processes available for nanowire growth are responsible to provide the ‘vapor’ of material for this growth mechanism. With the vapor transport technique the source material eg. *ZnO* is simply evaporated in a typically inert atmosphere and transported within a reactor to the substrate by diffusion or gas flow. Chemical vapor deposition uses reactive gases such as *SiH₄* to provide the source material, in this case *Si* in a temperature and pressure controlled reactor.

Although self-catalyzed growth has also been observed, the liquid phase exploited in VLS is typically provided by a metal catalyst deposited on the growth substrate [DL00, WDJ⁺09]. The material in the vapor phase can accumulate in the catalyst droplet until the concentration is supersaturated.

3 Experimental Methods

Preferential segregation of the excess material at the droplet-substrate interface leads to the growth of a nanowire. The size of the droplet can be used to control the diameter of the grown nanowire to some extent. An epitaxial relation between the substrate and the nanowire material may be used to direct the growth. Typical diameters and lengths for all the VLS nanowires used in this thesis are $50 - 300\text{ nm}$ and $> 5\text{ }\mu\text{m}$ respectively.

Figure 3.1: SEM images of the ZnO nanowire samples. In a) the dense samples grown via vapor transport on AZO are shown, while b) shows the sparser, PLD grown ZnO nanowires on a sapphire substrate.



Relatively dense ZnO nanowire samples are grown by vapor transport in Jena in the three-zone-furnace (3ZJ). The nanowires grow upstanding on a $\approx 500\text{ nm}$ layer of Al doped ZnO (AZO) sputtered onto a Si substrate, as shown in Figure 3.1a. The temperature at the 1 : 1 molar source mixture of ZnO and C was $1050\text{ }C^\circ$, the substrate position at 46 cm , Ar and O_2 flow 10 sccm each and the base pressure 7 mbar [BMS⁺06, Sti08, Mü09, Ogr13]. Further ZnO nanowire samples with a sparser lateral distribution of the upright nanowires on a sapphire substrate decorated with Au colloids are shown in Figure 3.1b. They were kindly provided from the University of Leipzig by Dr. Helena Franke. The parameters for the PLD growth of these samples are a laser power density of 2 J/cm^2 , 165 mbar base pressure at 40 sccm Ar flow, a substrate temperature of $900\text{ }C^\circ$ and a target-substrate distance of 35 mm [CZC⁺10]. For selected irradiation experiments, VLS grown Si -nanowires were used. These samples were kindly provided by Markus Glaser from the TU Vienna. They were grown epitaxially on a Si [111] wafer at 3 mbar and 515° in a low pressure chemical vapor deposition reactor (LPCVD) using Au colloids as a catalyst and monosilane/hydrogen atmosphere a source [LSH⁺08, JNW⁺15]. An SEM image of the VSL grown Si nanowires can be seen in Chapter 6.1, Figure 6.1.

3.2 Modification

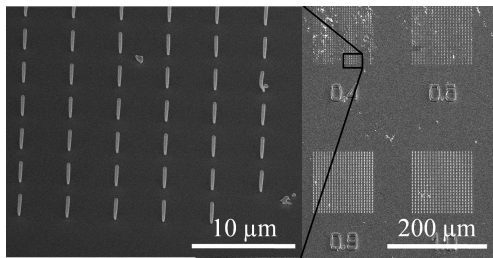


Figure 3.2: SEM images of the etched *Si* nanowire arrays. On the right, the numbers etched into the substrate under each array indicate the diameter in μm of the predefined *Ni* mask for that array.

Nanowires can also be synthesized “top-down” [HIK97, HKZ⁺10]. A “top-down” approach requires a predefined template, which is used to control the desired morphology. The *Si*-nanowire arrays used to study sputtering and plastic deformation within this dissertation were also kindly provided by Markus Glaser from the TU Vienna. They were etched by reactive ion etching (RIE) through a circular, e-beam lithographically defined *Ni* hard-mask, which set the nanowire diameter [JNW⁺15]. The RIE parameters were a flow of 50 *sccm* *SF*₆ and 100 *sccm* *O*₂ at a set pressure of 10 *mTorr* and a strike pressure of 30 *mTorr*. The radio frequency and inductive coupled plasma powers were 15 *W* and 100 *W*, respectively. The etching was performed at $-108\text{ }^{\circ}\text{C}$ for 5-15 *min*. After the RIE process, a 32 % *HCl* and (7:1)-buffered *HF* dip removed the *Ni*-hard mask and the oxide formed at the surface of the *Si*, respectively. Using this “top-down” etching process it is possible to prepare nanowires with diameters varying from 50 *nm* to 2 μm and a height of $\approx 3 \mu\text{m}$ on a single substrate for simultaneous irradiation. As seen in Figure 3.2, the spacing between the nanowires was larger than their height, so that there is no shadowing of the ion beam between the nanowires.

3.2 Modification

ROMEO

The ion irradiation for this dissertation was performed at the general purpose High Voltage Engineering implanter “ROMEO” at the IFK in Jena. It can provide an ion beam of virtually any element at energies ranging from 10 – 380 *keV*. The beam passes a 90° selector magnet and can be swept with

3 Experimental Methods

a frequency of $\approx 1\text{ kHz}$ to homogeneously irradiate areas up to several tens of cm^2 with ion currents of up to 1 mA . For this work ion current densities were limited to 500 nA/cm^2 , corresponding to $\approx 15\text{ min}$ for the typical fluence of 10^{16} ions/cm^2 .

Previous work has shown that nanowires can bend under ion irradiation [BSL⁺11, Bor12]. Therefore, a rotatable, heatable and tilted stage (RHT), illustrated in Figure 3.3, was custom built within the frame of this thesis, together with Stefan Noack [Noa14]. With it, bending of the upstanding nanowires can be avoided, because the nanowires are irradiated homogeneously from all sides at an angle of 45° . All the samples investigated in this thesis were rotated on the RHT and its preceding prototype sample stages during the irradiation.

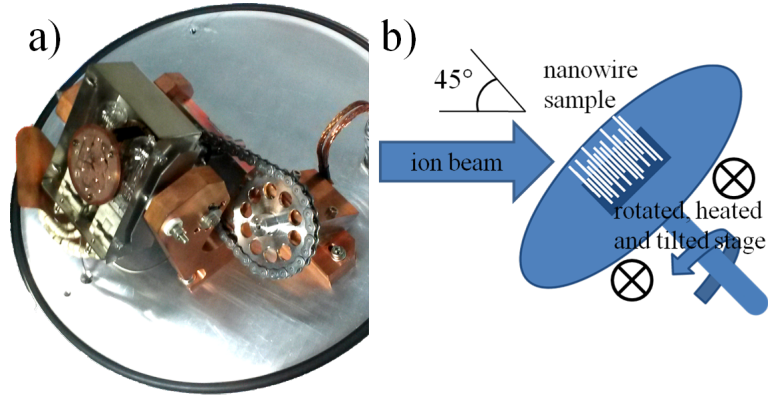


Figure 3.3: a) Foto and b) illustration of the rotated, heated and tilted (RHT) stage for the ROMEO implanter. The rotating stage is tilted towards the ion beam by 45° and heated from the back by two light bulbs. The temperature is controlled by a reference measurement on a stationary disk similar to the rotating stage, fixed beneath the light bulbs.

The sputtering and plastic deformation studies in chapters 4.3 and 6.2 were conducted with Ar^+ irradiation in Si nanowires to avoid any chemical effects of the incorporated ions. To prevent defect induced density changes and the Si nanowires from amorphizing, the irradiation temperature was 300° for the sputtering study. At this temperature the amorphization threshold be-

3.2 Modification

comes arbitrarily high [PMB04]. The other irradiations were performed at room-temperature. For the quantification of dopants in Chapter 5, ZnO -nanowires were irradiated with Mn^+ . Mn has a similar mass to Zn and both are medium-weight so that the linear cascade theory is applicable. Also, $ZnO : Mn$ is interesting as a possible material for diluted magnetic semiconductors (DMS) [Fur88, NKA⁺04]. Pragmatically, it is relatively easy to get a stable Mn^+ beam with ROMEO and with the quantification in mind, Mn is much less likely to be in any components at the XRF beamline and give a background than Fe, Co, Ni or Cu .

Focused ion beam - FIB

Some sample preparations required a FIB. These are highly specialized ion accelerators with the main objective of obtaining a small ion beam focus. Most of the systems use a Ga^+ beam and acceleration voltages up to 30 keV. The main use for FIBs is to sputter material extremely locally, making it a versatile tool for nano-machining. The FEI DualBeam Helios NanoLab 600i FIB system used for this dissertation is a scanning electron microscope (SEM) - FIB combination. The sample can thus be milled with the ion beam and investigated with the SEM reiteratively. The system is also equipped with a Pt -metal-organic gas injection system. The Pt containing organic molecule can be cracked locally on the sample by the secondary electrons created by either the electron or ion beam. Most of the Pt is deposited near the impact point of the primary beam at the substrate. However, typically a rather large ‘halo’ of minor Pt deposition can extend for a couple of μm . The FIB system can thus mill and deposit structures on a nm scale. For the sample preparation in this thesis all Pt deposition was done with the electron beam to avoid damage to the nanowire by the Ga^+ ion beam.

3 Experimental Methods

3.3 Characterization

Scanning Electron Microscope - SEM

The morphological changes in the nanowires were characterized by high resolution SEM in the FEI DualBeam Helios NanoLab 600i FIB system. The lateral resolution of the SEM system is $\approx 2\text{ nm}$. Images of individual nanowires were made before and after ion irradiation to quantify the sputtering. To find exactly the same place on the sample, a series of images with increasing magnification has to be made. Typically, images were made at an angle of 45° to the substrate with the alignment procedure the same before and after irradiation.

A semi-automated image analysis protocol was developed by Stefan Noack in his Master thesis [Noa14, JNW⁺15] to evaluate the SEM images of a large number of nanowires. It applies a (3x3) median filter to smooth out some noise and a Gaussian unsharp mask with $\sigma = 1\text{ px}$ and weighted at 60 % to resharpen the edges [San04]. An Otsu threshold [Ots79] is applied to separate the brighter nanowire from the darker background. Next, open source particle analysis software is used to find the main body of the nanowire and turn it upright, correcting any marginal tilt remaining in the SEM images [SACF⁺12, SPTS12]. Finally the sum of the gray-values in each line is used to calculate the diameter at that height along the nanowire axis. Because the investigated nanowires showed a characteristic bulge at the base, this point was used to align the height profiles of a single wire before and after irradiation. To avoid any irregular effects by the altered geometry at the top facet and the base of the nanowire, $\approx 20\%$ of the height was disregarded at either end of the extracted profile. After a fluence of 10^{16} cm^{-2} the change in diameter was close to the resolution limit of the SEM, therefore only the data for two subsequent irradiation steps of $2 \cdot 10^{16}\text{ cm}^{-2}$ ions was evaluated. A more detailed description of the image analysis process can be found in reference [Noa14] and the supplementary information of reference [JNW⁺15].

3.3 Characterization

Electron Back-Scatter Diffraction - EBSD

A Carl Zeiss Auriga CrossBeam Workstation fitted with an EBSD tool was used to identify whether nanowires remained crystalline after irradiation. The electron beam is focused on the sample at an arbitrary angle and the scattered electrons are detected by a large CCD detector in the SEM. Bragg diffraction along the crystal lattice planes produces a characteristic pattern of Kikuchi lines on the detector [Kik28, FH13] in crystalline samples. Amorphous or nano-crystalline samples show no pattern.

nano-XRF

Hard X-ray radiation stimulates the atoms within the radiated material to emit characteristic X-ray radiation. This X-ray fluorescence can be detected in an energy dispersive semiconductor detector and used to identify and quantify the elements in the sample [GS28]. In principle the method is similar to the more wide-spread energy dispersive X-ray spectroscopy (EDX), where an electron beam is used to excite characteristic X-ray fluorescence [JS82]. Very good lateral resolution can be obtained by having an EDX detector in a SEM. However, the advantage of using X-rays lies in the absence of Bremsstrahlung, which high energy electrons produce in matter in addition to characteristic X-rays. In XRF there is thus a much lower background and much lower concentrations of elements can be detected and quantified. Unlike normal X-ray tubes, synchrotron radiation is very brilliant, allowing it to be focused.

X-ray fluorescence with a nano-focussed X-ray beam (nano-XRF) was measured at the European Synchrotron Radiation Facility (ESRF), beamlines ID16b and ID13. The beamlines were run at various photon energies above 15 keV and with focal spot of typically $\approx 80\text{ nm}$ and $\approx 250\text{ nm}$ diameter, respectively. The nano-XRF thus allows the quantification of low concentrations with sufficient lateral resolution to resolve axial concentration gradients in a nanowire. Unfortunately, the resolution is not high enough to investigate radial distributions.

For this thesis, Mn irradiated ZnO nanowires were deposited on TEM grids either randomly by ‘imprinting’ or individually by using the micro-

3 Experimental Methods

manipulator in the FEI DualBeam FIB. Transferring individual wires requires some finesse, but it is possible to detach ZnO nanowires from their substrate without the Ga^+ FIB and to place them on the “lacey-carbon” TEM grids without any additional Pt deposition. In this way SEM images before and after irradiation of the same wire investigated by nano-XRF are available. At both beamlines the nanowires on the TEM grids are scanned under the fixed focal point of the X-ray beam with piezo-motors while the XRF spectra are collected with a Vortex EM silicon drift X-ray detector.

The spectra used for quantification were obtained in multiple scans across a nanowire at regular intervals along its length. Because the XRF signal can be used to locate the nanowire, only the points near the nanowire were measured with a high integration time and a low step-with ($< 1/2$ focal spot) to ensure a large number of counts ($> 10^5$ per scan) at reasonable measuring times.

nano-XRF quantification

The XRF-Spectra were evaluated using the open source PyMCA software package [SPC⁺07]. The effects of self absorption and excitation can be neglected, because the investigated nanowires are very thin compared to the X-ray absorption length, which is a couple of μm in ZnO . However, the detector-sample distance is responsible for an unavoidable attenuation length in air. Here, the X-ray absorption is dominated by Ar . Because Mn is relatively light, its characteristic X-ray emission at $K_{\alpha,Mn} = 5.9 \text{ keV}$ is absorbed more than the signal of the heavier Zn with $K_{\alpha,Zn} = 8.6 \text{ keV}$. Thus, absorption of the XRF signal in air has to be considered carefully in the fitting with PyMCA. The accuracy was double checked by measuring and quantifying trace elements in a calibration sample of bovine liver. In this way, optimal fitting parameters were found for each beam-time and applied to the respective spectra in the PyMCA batch mode.

Oxygen cannot be quantified in these beamlines, because its XRF emission is totally attenuated by air and a Si dead layer in the detector. The quantification of the Mn content in the ZnO nanowires thus relies on the assessment of the Mn/Zn ratio. In any case, it is a decent approximation to assume that

3.3 Characterization

the ZnO remains stoichiometric even during the irradiation. The samples are irradiated in a chamber with a base pressure $\approx 10^{-6} \text{ mbar}$, so according to the Hertz-Knudsen equation [Kol12] this will give a coverage of roughly one mono-layer or $10^{15} \text{ particles/cm}^2\text{s}$, if one assumes a sticking coefficient near 1. The maximum ion current density yields $10^{13} \text{ ions/cm}^2\text{s}$, so that an unlikely amount of preferential sputtering would be required to deplete the oxygen out of the wires. In addition, the wires will be oxidized in the normal atmosphere post irradiation. The Mn/Zn ratio is thus a good proxy for the Mn concentration.

The quantification limit can be estimated using a simulated XRF spectrum from PyMCA. By finding an appropriate photon flux and nanowire interaction volume, the simulation can reproduce the XRF spectrum with the actually measured number of counts at $K_{\alpha,Zn}$. The Mn content in the simulated matrix can then be decreased until the minimum Mn content is found that gives a signal at $K_{\alpha,Mn}$ just above the actually measured noise level. In this way a lower limit for the concentration resolution can be found at typically 0.1 % Mn/Zn .

4 Sputtering of Nanowires

The experiments presented in this chapter were conducted together with Stefan Noack and are partially published in his master thesis [Noa14] and in reference [JNW⁺15].

4.1 Simulation of the sputter yield

The sputtering of nanowires can be investigated by MC simulations using the software *iradina*. The discussion of the Sigmund sputter model in Chapter 2.1 concluded that a maximum is expected for a certain ion, ion energy and nanowire diameter combination. This is confirmed by MC simulations shown in Figure 4.1a and 4.1b for the examples of Xe^+ and Ar^+ ions, respectively, homogeneously irradiating a *Si* nanowire at an angle of 45° . In the simulations, the nanowire diameter and ion energy were both varied. The white line indicates the ion range of the respective ion in bulk calculated with SRIM and projected on to 45° . The maximum of the sputtering correlates very well with this ion range for both ion species. The heavy Xe^+ naturally has a much lower ion range than Ar^+ at the same ion energy. Also, sputtering is larger by about a factor of 2.5 for the denser collision cascades caused by the heavier Xe^+ ions.

In 4.1c, the sputter yield versus ion energy is extracted from the Xe^+ simulation for a set of fixed diameters. The black, red and blue curves correspond to the simulation of 25, 50 and 100 nm diameter wires, respectively. The corresponding vertical lines in Figure 4.1a show the position of the extracted data in the contour plot. The maximum clearly shifts to larger ion energies for larger nanowire diameters. The colored arrows indicate the ion energy for which the ion range, simulated by SRIM, is equal to the respective diameter.

4.1 Simulation of the sputter yield

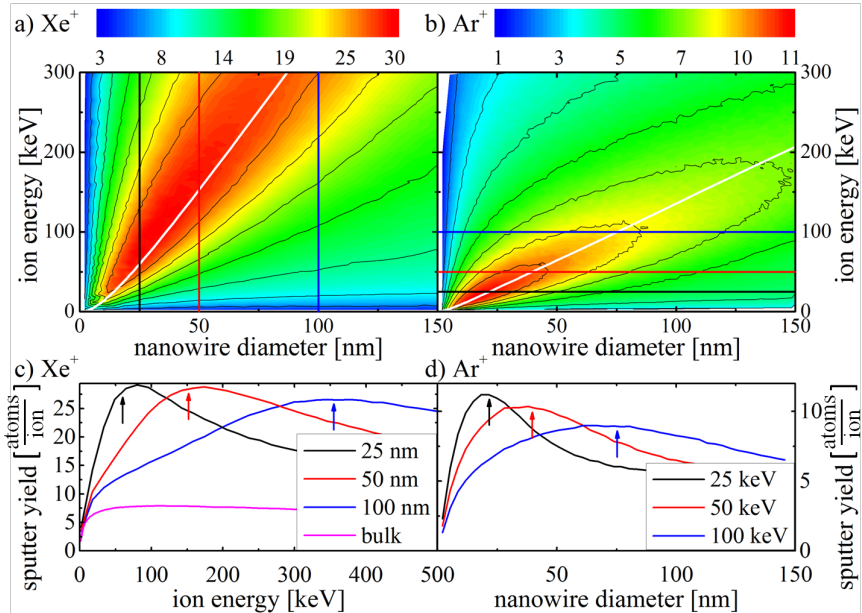


Figure 4.1: Contour plot of the sputter yield simulated with *iradina* for the irradiation with Xe^+ , a) and Ar^+ , b) ions of varying energy into *Si*-nanowires with varying diameters. The white lines indicates the respective ion's range in *Si* bulk at 45° , calculated with SRIM. The vertical lines in a) and horizontal lines in b) indicate where the sputter yields for a set of constant diameters c) and constant energies d) was extracted. In c) and d) the ion range in bulk is indicated with colored arrows.

The magenta curve shows the energy-dependent sputter yield for a flat *Si* surface irradiated with Xe^+ ions at 45° , simulated with *iradina*. The broad maximum sputter yield for this bulk simulation is found at $\approx 100\text{ keV}$. Correspondingly the global maximum sputter yield in nanowires is also found at $\approx 100\text{ keV}$ for 30 nm diameter wires.

Finally, in Figure 4.1d the sputter yield from Ar^+ irradiated *Si* nanowires is plotted as a function of the diameter for a set of fixed energies. Here, the black, red and blue curves correspond to 25, 50 and 100 keV ions and the arrows indicate the ion range at the respective energy. Again the maximum sputtering is found at a diameter corresponding to the ion range in bulk.

4 Sputtering of Nanowires

To relate this to the Sigmund sputtering model, with its Gaussian ellipsoid approximation of the damage profile, a Gaussian peak can be fitted to the recoil profile simulated with SRIM for both ions in *Si* [BZH12]. The so found mean damage depth is constantly around 0.7 times the ion range for the whole energy range investigated here. A naive first approximation with the Sigmund sputtering model would predict that the sputtering is maximal where the ions energy is such, that the mean depth of the damage and the radius of the irradiated nanowire coincide. However, this is only true for central impacts, while the simulated situation is an average over all ion-nanowire impact parameters. For non-central impacts there is less of the nanowire ‘in front’ of the ion’s path. Therefore, the maximum of the sputter yield is also at lower energies than it would be for solely central impacts. It is thus a consequence of the irradiation geometry that the diameter of maximum sputtering is equal to the projected ion range and not the mean depth of the damage distribution. To test the limits of the Sigmund model, a more thorough investigation of the Sigmund model’s predictions for various irradiation scenarios may be interesting; however, because the MC simulations reproduce the reality more realistically anyhow, it will not be undertaken here.

4.2 Redeposition

While irradiating a nanowire which is standing perpendicular on a substrate, as is the case in the samples shown in Figure 3.2, material will also be sputtered from the substrate. Some of the sputtered material from the substrate will be redeposited on the nanowire, so that the observable sputter yield will be lower than the actual sputtering from the nanowire. The following calculation will estimate how many atoms are redeposited on the nanowire per irradiated ion fluence on the substrate. Consider the situation shown in Figure 4.2. An ion hits the substrate at point A . A possible path of a sputtered atom is indicated by the red line to a point on the nanowire, where the substrate atom is redeposited on the nanowire.

First, the probability P of a sputtered atom to hit the nanowire is calculated:

$$P = \int_0^{2\pi} \int_0^{\pi/2} H(\theta, \varphi, r, R, L) \tilde{SY}(\theta, \varphi) \cos(\theta) d\theta d\varphi, \quad (4.1)$$

where $H(\theta, \varphi, r, R, L)$ is the probability distribution of hitting the nanowire. It is normalized to $1/4\pi$ if the trajectory along θ and φ from A hits the nanowire with length L and radius R , and zero otherwise. For irradiation at an angle, the angle distribution of the sputter yield $\tilde{SY}(\theta, \varphi)$ is expected to have a preferential direction along the ion beam [VWMS08]. However, the effective distribution becomes rotationally symmetric (independent of the angle φ) if

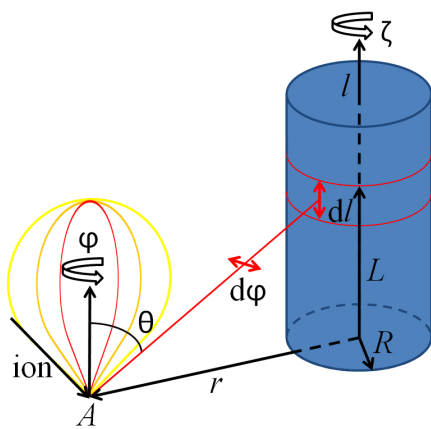


Figure 4.2: Illustration of the redeposition of sputtered material from the substrate point A onto the nanowire with radius R at a height L . Because the wire is rotated around its axis ζ and the whole substrate is irradiated, a rotationally symmetric angle distribution for the sputtered atoms can be chosen.

4 Sputtering of Nanowires

one neglects the shadowing of the ion beam on the substrate by the nanowire. Then all points around the wire are hit, and the wire is rotated around its axis (angle ζ), so that an effective, rotationally symmetric angle distribution $\tilde{SY}(\theta)$ of the sputtered atoms from the substrate can be used, as indicated by the yellow, orange and red bulbs in Figure 4.2. A $\cos^\kappa(\theta)$ distribution is chosen:

$$\tilde{SY}(\theta) = \frac{SY \cdot \cos^\kappa(\theta)}{\int_0^{2\pi} d\tilde{\varphi} \int_0^{\pi/2} \cos^\kappa(\tilde{\theta}) \cos(\tilde{\theta}) d\tilde{\theta}} = \frac{SY}{c(\kappa)} \cdot \cos^\kappa(\theta), \quad (4.2)$$

where the denominator $c(\kappa)$ normalizes the angle distribution function $\cos^\kappa(\theta)$ and SY is the total sputter yield from the surface. Because it forms a flattened angle distribution for $\kappa < 1$, this increased emission of atoms at larger angles θ can emulate the rotation of a slanted angle distribution.

The parametrization of $H(\theta, \varphi, r, R, L)$ in φ is straightforward, because the integration bounds for φ are $[-\gamma, \gamma]$ with $\gamma = \arcsin(R/r)$ the angle between r and the tangent to the nanowire in Figure 4.3a. To solve the integration over θ , it is useful to express the distance q from the impact point to the base of the nanowire as a function of $\rho = R/r, r$ and φ :

$$q(\rho, r, \varphi) = r \cdot \sqrt{1 + \rho^2 - 2\sin^2(\varphi) - \sqrt{\cos^2(\varphi)(\cos(2\varphi) - 1 + 2\rho^2)}}. \quad (4.3)$$

Then the integration over θ can be substituted by an integration over the length of the nanowire l . The substitution can be found looking at Figure 4.3b:

$$\begin{aligned} d\theta &= \frac{\sin(\theta)}{\sqrt{L^2 + q^2}} dL, \\ \theta &= \arctan(q/L). \end{aligned}$$

Inserting into equation 4.1 and simplifying yields:

$$P = \frac{2 SY}{c} \int_0^\gamma \int_{L_1}^{L_2} \frac{l^{\kappa+1} q}{(l^2 + q^2)^{(\kappa+3)/2}} dl d\varphi. \quad (4.4)$$

4.2 Redeposition

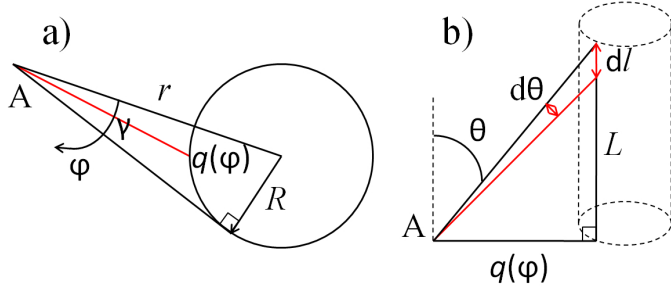


Figure 4.3: a) Top view: R is the radius of the nanowire, r the distance from the point of impact A to the center of the wire and $q(\phi)$ the distance to the wire's surface at the base of the wire. The angle between r and the tangent to the nanowire circumference is γ . b) Side on view: θ is the angle to the substrate normal of the trajectory of a sputtered substrate atom to hit the wire at L .

With $l^* = L_1 - L_2$, the area hit on the nanowire is now $\pi R l^*$, positioned at the height $L = (L_1 + L_2)/2$ as indicated between the two red lines in Figure 4.2. Next, the probability P to hit the nanowire at each substrate position is integrated over the whole substrate area and normalized to the area of the nanowire which is hit. This yields the fluence of atoms Θ hitting the nanowire at height L per irradiated ion fluence Φ :

$$\frac{\Theta}{\Phi} = \frac{2 SY}{c\pi R l^*} \int_0^{2\pi} d\zeta \int_R^\infty \int_{L_1}^\gamma \int_{L_2}^{L_1} r \frac{l^{\kappa+1} q}{(l^2 + q^2)^{(\kappa+3)/2}} dl d\varphi dr. \quad (4.5)$$

The integration can be solved using the numerical integration tools CQUAD and QAGI [Gou09]. Perhaps counter-intuitively, the result is independent of the nanowire radius R and the height L for which the deposition is calculated. For the generous estimation of a very broad distribution when $\kappa = 0.25$, the redeposition amounts to only $\Theta = 10\% \cdot \Phi \cdot SY$. As already shown in Figure 4.1c, the sputter yield is significantly lower from the plane substrate than from the nanowire. Therefore, the redeposition can be safely neglected for the evaluation of sputtering. However, redeposition may remain relevant to substrates of a different material than the nanowire, where the incorporation of substrate atoms in the nanowire has detrimental doping effects. Because the atoms sputtered from the substrate have a very low energy, they will be

4 Sputtering of Nanowires

deposited on the surface of the nanowire. This position at the surface of the nanowire makes them prone to re-sputtering, which reduces the finally incorporated number of substrate atoms further. Nevertheless, keeping the redeposition in mind is advised in choosing the substrate material.

4.3 Si nanowire sputtering by Ar⁺ irradiation

The experimental verification of the diameter-dependent maximum in sputtering was investigated on etched *Si*-nanowire arrays. Figure 4.4a shows the principle irradiation setup illustrated by a SEM image of a single nanowire before and after the irradiation with 300 keV Ar⁺. The etched nanowire samples and the RHT allowed the simultaneous, rotated irradiation of upstanding nanowires with various diameters at 300 °C. Figure 4.4b shows the extracted and aligned diameter versus height profile for the nanowire in Figure 4.4a. More than a hundred such profiles were semi-automatically extracted for many different nanowire diameters from SEM images made before and after two separate ion irradiation steps with an ion fluence of $2 \cdot 10^{16} \text{ ions/cm}^2$. The sputter yield calculated from these extracted profiles is plotted versus the local diameter in 4.4c for 100 and 300 keV Ar⁺.

The experimental sputter yield reproduces the qualitative, simulated diameter dependence of the sputter yield well. The experimental values are, however, lower than the simulation results by 2-4 in absolute sputter yield or roughly a factor of 2. For 100 keV Ar⁺ ions the sputter yield is largest in $\approx 60 \text{ nm}$ diameter nanowires and decreases quickly with increasing diameters. With 300 keV Ar⁺ ions a broader maximum arises at diameters of $\approx 170 \text{ nm}$. For both ion energies the maximum sputtering is found for those nanowire diameters where the diameter is similar to the ion range, just as discussed in Chapter 4.1 and the Sigmund sputtering model in Chapter 2.1.

The fact that the experimentally observed sputter yield has its maximum at slightly lower diameters than the simulated values for both the 100 keV and 300 keV irradiations may indicate the occurrence of cluster and thermal sputtering. Both have been predicted with MD simulations [NSUM14, UBNM15, ABU15], albeit in nanostructures with much smaller dimensions. Because the

4.3 Si nanowire sputtering by Ar⁺ irradiation

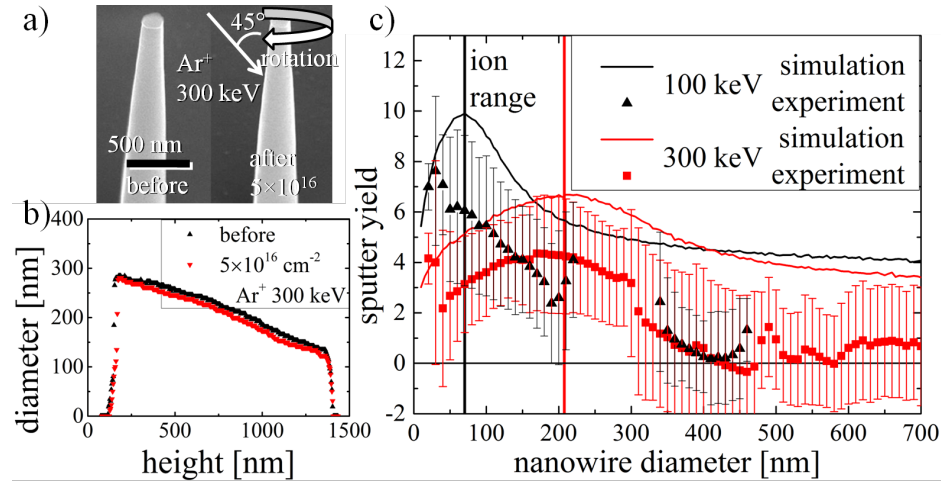


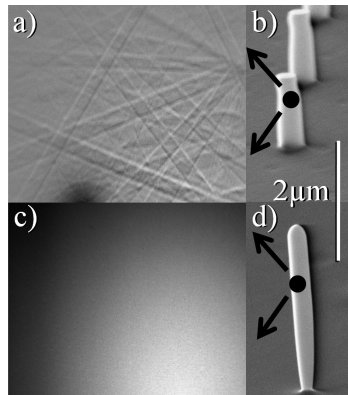
Figure 4.4: a) Exemplary SEM images of a Si nanowire before and after the rotated irradiation with 300 keV Ar⁺ at 300°C. The extracted diameter vs. height profile for this nanowire is shown in b). From many such profiles the sputter yield vs. diameter was calculated and plotted in c) as black triangles and red squares for the irradiation with 100 and 300 keV Ar⁺, respectively. The ‘error bars’ indicate the variance of the data points grouped together every 10 nm. The sputter yield calculated with *iradina* simulations is shown for either case as a line-plot. The corresponding SRIM ion range at 45° is marked by a vertical line.

kinetic energy of the ion is, on average, distributed to less material in nanowires with smaller diameters, both cluster and thermal sputtering increase for decreasing nanowire diameters.

The interruptions and discontinuities for diameters < 50 nm, at ≈ 200 nm, ≈ 300 nm and ≈ 500 nm are located where the diameter range of an array of nanowires on the irradiated substrate ended. Here, there are fewer (none for 100 keV at ≈ 200 – 300 nm) nanowires which could be evaluated. The large variance indicated in Figure 4.4c as ‘error-bars’ can be attributed to the fact that the observed diameter changes of approximately 5 nm are close to the resolution limit of the SEM, which is 2 nm. Therefore, the observation of a reasonable sputter yield value for one diameter is only possible with the large sample number, > 1000. This problem could be reduced by increasing the

4 Sputtering of Nanowires

Figure 4.5: The Kikuchi pattern a) clearly shows that the nanowire, shown in the SEM image b), has remained crystalline during the irradiation at 300°C . The lack of any structured signal in c) shows that the nanowire irradiated at room-temperature, shown in the SEM image d), was amorphized.



ion irradiation fluence step size, so that there is a larger difference between the nanowire diameters before and after ion irradiation. However, this would invariably increase the variance in the mean diameter for which the sputter yield is determined. Before the irradiation an approximation using the simulated sputter yields was made to find an optimum ion fluence step size, but with the low sputter yield observed in the experiment the chosen ion fluence steps of $2 \cdot 10^{16} \text{ ions/cm}^2$ are on the low side.

Sputter yields around 0 atoms/ion , as found in the experimental values at 400 nm , are not realistic. They have to be attributed to misalignment and remaining focal plane, brightness and contrast differences between the SEM images before and after irradiation, which could not be corrected in the image analysis. These differences introduce systematic deviations, which may be different from one nanowire array to the next. Therefore, the variance is a more sensible estimation at the overall accuracy of the experimentally determined sputter yield than the more usual standard deviation. Because of the large number of investigated nanowires, the standard deviation is so small that it would disappear behind the data points in the graph and overestimate the actual experimental accuracy considerably.

The quantitative discrepancy between the simulated sputter yield and the experimental values is not unexpected. To start with, the quantitative value from the *iradina* simulation is questionable (Chapter 2.2). In the experimental values, any effect of incorporated defects, or even amorphization, on the density of the *Si* in the nanowires can be confidently discarded, because nano-

4.4 Summarizing discussion

wires remained crystalline during the irradiation even up to the high fluence of $5 \cdot 10^{16} \text{ cm}^2$. This was expected from irradiation studies found in literature [PMB04] and confirmed by EBSD (Figure 4.5). The main contribution to a systematic deviation in the experimentally evaluated sputter yields is the oxidation of the *Si* nanowires in air between the subsequent irradiation and SEM investigation steps. The thickness of oxidized *Si* on the surface of the nanowires is substantial but dependent on uncontrolled factors such as humidity and temperature [Luk72, ABORvdBA91]. It can be estimated to amount to around 2-5 nm. Because all the oxygen in the oxidized layer of the nanowires has to be sputtered away additionally, the experimental procedure will substantially underestimate the sputter yield.

4.4 Summarizing discussion

The sputter yield was investigated with MC simulations *Si*-nanowires irradiated at 45° with Xe^+ and Ar^+ , varying the ion energy and nanowire diameter. It shows a local maximum in the energy and diameter-dependent sputtering where the energy-dependent ion range is about equal to the diameter of the nanowire. This can be understood as the point where the overlap of the nuclear energy loss and the surface of the nanowire is largest. For a fixed ion energy the ion will pass through nanowires with a small diameter, limiting the amount of energy deposited, as well as the surface area effected by nuclear energy loss. For increasing diameters, both the surface area and deposited energy increase, until the diameter is so large that the collision cascade no longer reaches the back side of the nanowire and forward sputtering is suppressed. Qualitatively this confirms that the Sigmund sputter model provides a reasonable understanding for the diameter and energy dependence of sputtering in nanowires. These sputtering results are in line with the results of Urbassek et al. published in reference [UBNM15]. Unfortunately, Urbassek et al. investigate the Sigmund model analytically only for nanowires with a radius larger than the ion range, so that the diameter-dependent maximum in the sputter yield is not discussed in this context. The MC simulations in the same reference, however, cover a large range of ion range to nanowire diameter

4 Sputtering of Nanowires

ratios and a diameter-dependent maximum in the sputter yield is also found for diameters comparable to the ion range.

The theoretical predictions were confirmed in experiments on the sputtering of Ar^+ irradiated, etched *Si* nanowire arrays. From high resolution SEM images performed before and after the irradiation the diameter-dependent sputter yield could be extracted for the irradiation at 100 and 300 keV. A quantitative reproduction of the simulated sputter yields is not possible because of limits in both the simulation and experimental accuracy, however, these experiments reliably reproduce a maximum in the diameter-dependent sputtering, albeit at slightly lower nanowire diameters. Finding the maximum at lower nanowire diameters in the experiment than in the simulation, may indicate that thermal and cluster sputtering occur. Both would enhance sputtering for small nanowire diameters but are not included in the *iradina* simulation. Increased sputter yields because of thermal effects are, observed in the MD simulations published by Urbassec et al. [UBNM15] for a very similar scenario. Unfortunately, only small nanowire radii were investigated and the shift of the maximum sputter yield to lower nanowire diameters because of thermal effects is not confirmed. That thermal evaporation and cluster emission can play a large role in sputtering is confirmed conclusively in other experimental investigations [GHB⁺13, IKN⁺14, ABU15, JHMR15]

A theoretical investigation into the redeposition of sputtered material from the substrate onto the nanowires produced an estimation of the number of substrate atoms sputtered onto the nanowires. It was shown that the redeposition is negligible for the quantification of sputtering, nevertheless it may have to be considered in other studies involving the irradiation of nanowires. Significantly, the redeposition is neither dependent on the nanowire radius nor the height at which the surface atoms are deposited. Therefore, redeposition cannot account for the fact that the experimentally observed diameter of maximum sputtering is lower than theoretically predicted.

5 High Doping Concentrations in Nanowires

High ion fluences are needed to achieve high doping concentrations in a given structure. The simulations and experiments presented in this chapter were all performed with $175\text{ keV }Mn^+$ irradiated ZnO nanowires with approximately 200 nm diameter; however, the conclusions also apply to other material combinations and structures. Some of the results presented in this chapter are also published in reference [JNP⁺14].

5.1 Doping and Sputtering

With *iradina* the distribution of the places where the ions come to rest gives the profile of the concentration of dopants per ion fluence. Locally the concentration [atoms/cm^3] increases a certain amount per fluence [ions/cm^2], leading to the somewhat awkward unit of for the doping efficacy [$(\text{atoms}/\text{cm}^3)/(\text{ions}/\text{cm}^2)$]. An example of the dopant distribution simulated with *iradina* is shown in Figure 5.1a for the irradiation of a 200 nm ZnO nanowire with $175\text{ keV }Mn^+$. The ions enter the y - z plane at random locations and at an angle of 45° to the z -axis, which is periodically continued outside the plane of the image. It is clear that a homogeneous doping profile is not easy to obtain for the irradiation of a nanowire from one side. As with the creation of a box profile in bulk irradiations, multiple irradiation steps with varying energies are required. Note that an ion energy of 175 keV is obviously not enough to permeate the whole nanowire diameter of 200 nm , so that an additional irradiation with higher ion energy would be required to obtain homogeneous doping. Rotating the nanowire under the ion beam is a much easier way of increasing the

5 High Doping Concentrations in Nanowires

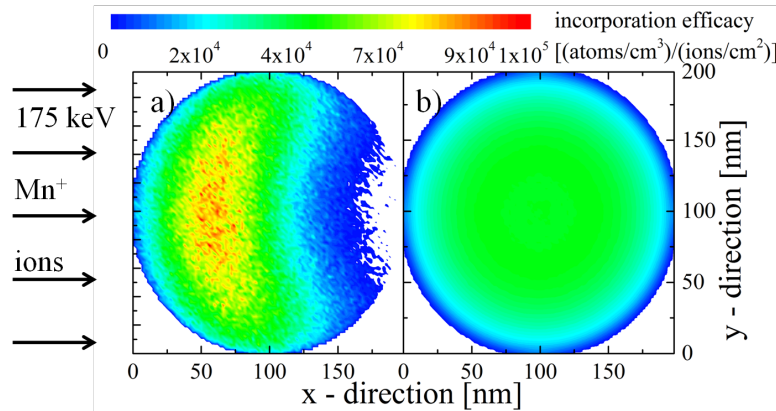


Figure 5.1: a) Color plot of the concentration per ion fluence for the irradiation of a 200 nm ZnO nanowire with 175 keV Mn^+ ions at an angle of 45° to the z -axis. The energy was selected so that the rotation of this profile produces a radially homogeneous dopant distribution, as shown in b). The mean dopant incorporation efficacy is $3.6 \cdot 10^4$ $(\text{atoms}/\text{cm}^3)/(\text{ion}/\text{cm}^2)$ in both cases.

homogeneity of the doping profile. Figure 5.1b shows the local dopant incorporation efficacy for the rotation of the profile shown in 5.1a. Irradiation with a single, relatively low ion energy produces a homogeneous doping profile.

Because lower energy ions have lower ranges, there are fewer paths that cause the ion to leave the nanowire, particularly in the forward direction. Therefore, the first advantage of decreasing the ion energy is that the doping efficacy is larger for lower ion energies, so a lower irradiation ion fluence is required to achieve doping at a desired concentration. Furthermore, lower ion energy impacts also produce less damage in the irradiated matrix. Together with an optimal irradiation temperature, the rotated irradiation was utilized to improve the magnetic properties of Mn^+ irradiated $GaAs$ nanowires in references [BMB¹¹, PKB¹², Bor12, KPJ¹³, PKJ¹⁴].

5.2 nano-XRF on single nanowires

The increase in doping concentration with the irradiated ion fluence was investigated on ZnO nanowire samples grown in Jena. The samples such as

5.2 nano-XRF on single nanowires

the one shown in Figure 3.1a show an upstanding, dense forest of nanowires on the growth substrate. The nanowires were rotated during the irradiation with $0.24, 0.48, 0.95$ and $1.9 \cdot 10^{17} \text{ ions/cm}^2 \text{ Mn}^+$ ions at 175 keV ; corresponding to Mn/Zn ratios of $0.02, 0.04, 0.08$ and 0.16 , as extrapolated from the mean doping efficacy obtained from the *iradina* simulation. After the irradiation, they were transferred onto the *C*-foil of a *Cu*-TEM grid by imprinting.

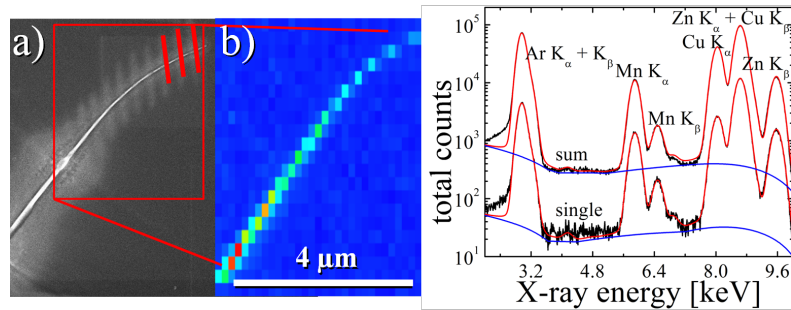


Figure 5.2: a) SEM image of a $175 \text{ keV} \text{ Mn}^+$ irradiated ZnO nanowire on the carbon-foil of a Cu TEM grid after XRF investigation. The red lines indicate where the focused X-ray beam was scanned with a long integration time. b) Intensity map of the X-ray signal from the nanowire shown in a). The black lines in c) show exemplary measured XRF-spectra of a single scanned line and for the sum of all the lines for the nanowire shown in a) and b). The fitted background and XRF-spectra are shown by blue and red lines.

Figure 5.2a shows a SEM image of one of the Mn^+ irradiated ZnO nanowires after investigation by nano-XRF at the ESRF. The nanowire shows some damage at one point where the exposure to the XRF-beam was accidentally prolonged during the navigation on the sample. Also the track of the intense, focused X-ray beam can be seen on the carbon foil by some redeposition of material. All in all, the damage to the nanowire is, however, not large enough to have an effect on the quantification, especially considering that this particular nanowire was selected because it showed the most pronounced effects. In Figure 5.2b a map of the detected X-ray intensity clearly shows the nanowire. The XRF spectrum collected for one of the scans indicated in the SEM image 5.2a is shown in 5.2c. The number of counts for a single scan is comfortably

5 High Doping Concentrations in Nanowires

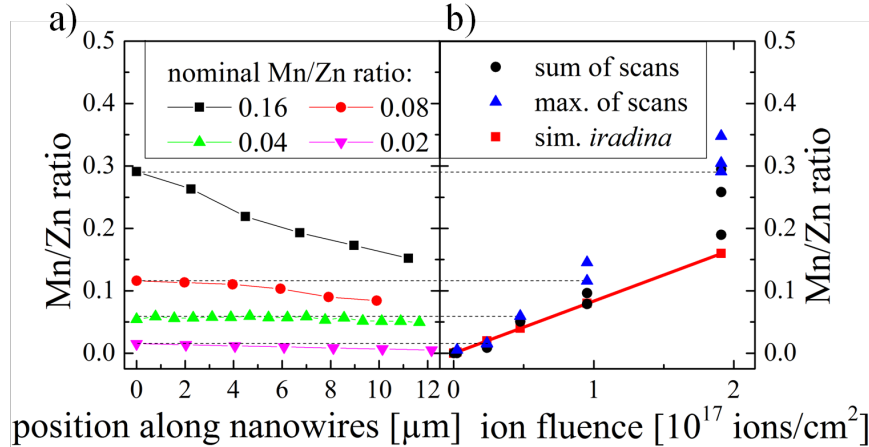


Figure 5.3: a) Mn/Zn ratio quantified with PyMCA for representative wires along the length of the nanowires for varying nominal concentrations. The tip of the nanowires is found at $0\ \mu m$. In b) the black circles show the average ratio obtained for various nanowires by fitting to the sum of all scans. The blue upturned triangles show the maximum ratio found along the length of the nanowires. The corresponding data points in the plot of the concentration versus the length of the nanowire in a) are connected with a dashed line. The red data points and line in b) indicate the linear extrapolation to the nominal Mn/Zn ratio from *iradina* simulations.

sufficient to quantify the Mn and Zn content. The average concentration for a nanowire was determined by fitting the sum XRF-spectrum of all scans across the nanowire.

In Figure 5.3a the Mn/Zn ratio is plotted over the position along the nanowires' length for the four nominal concentrations. Clearly, there is a significant gradient in the Mn concentration along the nanowire length. The maximum Mn/Zn ratio was always found at the tip of the nanowires. The tip of the nanowires could be identified in the SEM images by the tapering of the nanowires. The Mn/Zn ratio for both the sum of all scans, as well as the scan at the tip showing the maximum Mn/Zn ratio, is plotted in 5.3b alongside the nominal ratio extrapolated from *iradina* simulations.

5.2 nano-XRF on single nanowires

Two pieces of information can be gained from these results. First, the nanowires on the sample clearly shadowed each other from the ion beam, leading to the pronounced Mn concentration gradient along the wires' length. The shadowing is least at the tips of the nanowires, therefore these points correspond closest to the simulated situation. The shadowing also causes a tapering of the nanowires towards the tip, because the material sputtered away increases with increasing exposure to the ion beam. The second point is that the increase in Mn concentration per ion fluence is much stronger than the linear extrapolation from static simulations. Using the doping efficacy gained from the earlier simulations to calculate the required ion fluence for a desired doping concentration assumes, that the concentration increases linearly with the irradiated ion fluence. However, this is only true in the absence of sputtering. Sputtering erodes the target nanowire at the same time as ions are incorporated. It thus leads to a non-linear increase in the concentration of dopants with the irradiated ion fluence. To separate the effect of shadowing amongst the nanowires from the sputtering of each individual nanowire, the irradiation and quantification has to be repeated with nanowires with a sparser lateral distribution, as shown in Figure 3.1b. These were kindly provided by Dr. Helena Franke from the University Leipzig.

The same nano-XRF quantification procedure was followed to investigate the Mn/Zn ratio after the irradiation of these sparser nanowire samples with 0.25, 0.5, 1 and $2 \cdot 10^{17} \text{ ions/cm}^2$ of 175 keV Mn^+ . The results are shown in Figure 5.4. The Mn/Zn ratios plotted against the nanowire length in 5.4a no longer show any gradient. The Mn/Zn ratio for the nanowires irradiated with higher ion fluences shows a significant spread because the thinned nanowires have a much smaller volume and thus give a lower total XRF signal. Added to this, the thinner wires could only be attached to the lacy carbon loosely, so that they drifted much more during the XRF scans making it impossible to increase the integration time significantly to compensate for the lower signal.

As shown in Figure 5.5, these wires were individually transferred to the lacy carbon TEM grid so that nanowires, which were investigated by SEM before and after irradiation, could be selected. For example, the diameter of the nanowire irradiated with the highest ion fluence was reduced from 202 nm

5 High Doping Concentrations in Nanowires

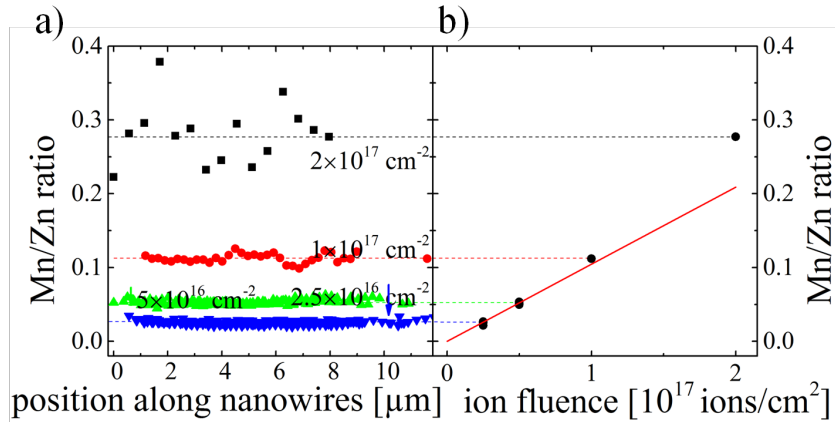


Figure 5.4: a) Mn/Zn ratio along the wire length for sparse nanowire samples irradiated with the indicated ion fluence of 175 keV Mn^+ . There is no concentration profile along the wire length. In b) the average ratio obtained by fitting to the sum of all scans for the respective ion fluence is shown. The red line in b) shows the linear extrapolation from *iradina* simulations.

to 93 nm by sputtering. The nanowires irradiated with lower ion fluences showed lower reductions in their diameters, as expected. From these diameter reductions the sputter yield can be calculated, resulting in sputter yields in the range of 5 - 20 atoms/ion. As seen in the dedicated study of sputtering in Chapter 4.3, these values have a very large spread.

The determined average Mn/Zn ratio is plotted in 5.4b against the irradiated ion fluence for all irradiated fluences. It is accurate to within ± 0.01 , because it is based on the sum of the spectra of all the individual scans. This sum-spectrum includes a sufficiently large number of counts in all instances. The initial increase in the Mn/Zn ratio with the irradiated ion fluence closely follows the linear extrapolation from the doping efficacy for fluences up to $0.5 \cdot 10^{17} \text{ ions/cm}^2$. This is an important result, because it confirms that the MC BCA simulation can accurately predict the incorporation of dopants quantitatively. Therefore, the doping efficacy is a useful number to determine the required ion fluence for a desired doping concentration for low ion fluences, where sputtering is not yet significant. However, as with the

5.3 Pseudo-dynamic simulation

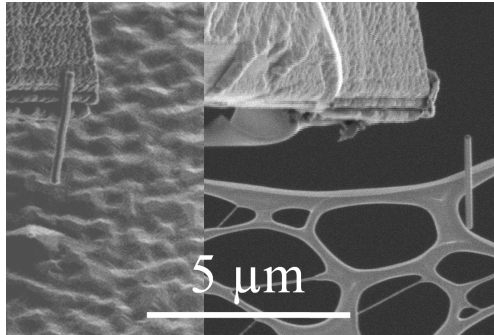


Figure 5.5: SEM images showing a ZnO nanowire broken off the growth substrate (left) with a micro-manipulator and transferred onto the lacy carbon-foil on a commercial TEM grid (right). Using this technique, individual nanowires investigated by SEM before and after the irradiation could be selected for subsequent nano-XRF quantification.

denser nanowire sample, for high ion fluences the increase in the Mn concentration is much larger than the simple linear extrapolation from the *iradina* simulation. The fact that there is no longer a gradient in the concentration along the nanowire length for the sparser samples confirms that the previously observed, strong gradient in the incorporation was caused by the shadowing of the nanowires amongst themselves.

5.3 Pseudo-dynamic simulation

The direct simulation of the effect of sputtering on the incorporation of dopants into nanowires requires a dynamic simulation program which also considers the three dimensional geometry of the target. Because such software is currently not openly available, a step-by-step investigation using results from static simulations will be undertaken to discuss the observed interaction between dopant incorporation and sputtering.

The most straightforward approach is to consider the total sputter yield and the doping efficacy to be constant. With these assumptions and a reiterative calculation of incremental ion fluence steps, a pseudo-dynamic simulation can be numerically constructed. The Mn concentration increases with each irradiated incremental ion fluence step by the value determined by the doping efficacy. Then the number of Zn , O and Mn atoms is reduced by sputtering

5 High Doping Concentrations in Nanowires

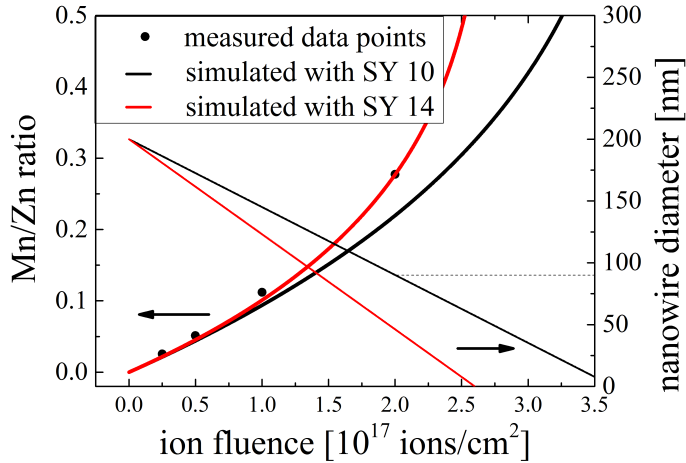


Figure 5.6: Plot of the Mn/Zn ratio (left axis) versus the irradiated ion fluence of $175 \text{ keV} Mn^+$ for the measured nanowires and two simulations using different sputter yields. The nanowire diameter (right axis) is also plotted against the ion fluence for both simulations. The dashed line at 90 nm marks the final radius of the data point corresponding to the highest irradiated fluence.

in such a way, that the total sputter yield is divided between $Zn + O$ and Mn according to the current Mn concentration. The total number of atoms is used to calculate the new nanowire radius and the next incremental ion fluence step can be calculated.

Figure 5.6 shows the experimentally determined Mn/Zn ratios next to such a simulation. The doping efficacy was set to the same value used for the linear extrapolation: $3.6 \cdot 10^4 \text{ (atoms}/\text{cm}^3\text{)}/(\text{ion}/\text{cm}^2)$. The total sputter yield was set to 10 atoms/ion for the simulation yielding the values depicted in black. This sputter yield value corresponds to the sputter yield determined from the reduction in the radius of the nanowire irradiated with $2 \cdot 10^{17} \text{ ions}/\text{cm}^2$ and therefore, unsurprisingly, this simulation produces the the correct diameter of $\approx 90 \text{ nm}$ at this ion fluence. However, the calculated Mn/Zn ratio is too low. Conversely, a simulation with a larger sputter yield of 14 atoms/ion , indicated in red, correctly reproduces the Mn/Zn ratio, but erodes the nanowire too quickly. Nevertheless, the overall agreement between the experiment and the simulation seems promising and confirms that the super linear increase in

5.3 Pseudo-dynamic simulation

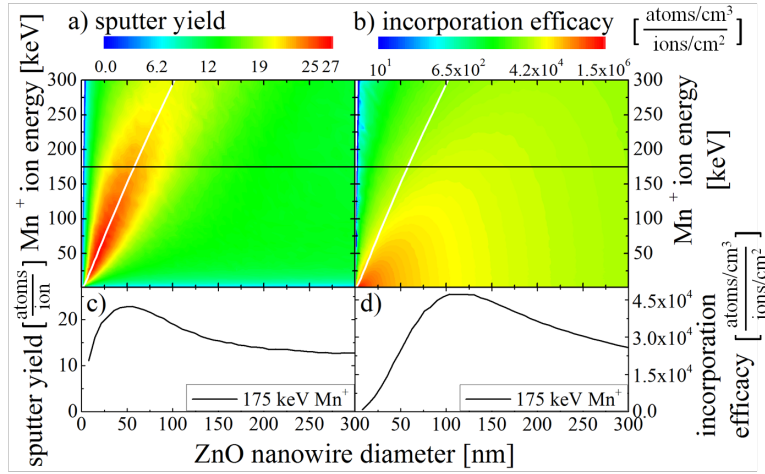


Figure 5.7: a) Sputter yield for the irradiation with Mn^+ of ZnO nanowires with varying diameters and ion energies. From the same simulations the dopant incorporation efficacy was determined and plotted in b). The white line in both plots indicates the ion range at the respective energy and 45° , calculated with SRIM for Mn^+ in ZnO . The horizontal black line indicates the ion energy used in the experiments and simulations in this Chapter. For this energy the diameter-dependent sputter yield and doping efficacy are plotted in c) and d) respectively.

the doping concentration observed in the experiment can be explained by the sputtering of the nanowire.

To increase the accuracy of the pseudo-dynamic simulation, results from a set of static simulations for varying diameters can be used. The sputter yield is dependent on the nanowire radius and the ion energy as shown in Figures 5.7a and 5.7c. This relation is discussed in detail in the previous Chapter 4.1. Likewise, the incorporation efficacy plotted in 5.7b is also dependent on the nanowire radius and the ion energy. For a fixed diameter and increasing ion energy the efficacy is monotonically decreasing, because the probability of the ion to leave the nanostructure rises together with the ion range. For a fixed ion energy, as shown in Figure 5.7d, the probability of an ion to stay in the nanostructure increases with increasing nanowire diameter, so that for small diameters the efficacy also increases with increasing diameter. For large diameters this effect is overcompensated by a stronger dilution of the dopants

5 High Doping Concentrations in Nanowires

in the volume of the nanowire which increases as the square of the diameter. This leads to a maximum in the incorporation efficacy at diameters around twice the ion range. Note that the color scale in 5.7b is logarithmic, while the graph 5.7d has a linear scale.

The numerical, pseudo-dynamic simulation can easily be adapted to use the diameter-dependent values for the sputter yield and the dopant incorporation efficacy of Figures 5.7c and 5.7d. As with the previous pseudo-dynamic simulation, which only considered constant sputtering and dopant incorporation efficacy, it is only possible to reproduce the correct diameter *or* the Mn/Zn ratio. For the results shown in Figure 5.8 the diameter-dependent sputter yield used for the simulation had to be halved. A simulation with the full sputter yield shown in Figures 5.7c already eroded the 200 nm nanowire completely after the irradiation with an ion fluence of $\approx 1.5 \cdot 10^{17} \text{ ions/cm}^2$. This is not a cause for concern, however, because the quantitative values for the sputter yield obtained by *iradina* simulations are not expected to be reliable and the effective sputter yield will be reduced in a material which can (re)-oxidize. Both these points were already discussed in Chapter 4.

The resulting Mn/Zn ratios from such a simulation are plotted in Figure 5.8 as red squares. The stronger than linear increase in the Mn/Zn ratio with the irradiated ion fluence is offset by the doping efficacy decreasing markedly with increasing ion fluence from $\approx 1.5 \cdot 10^{17} \text{ ions/cm}^2$. Here, the nanowire has a remaining diameter of around 120 nm. At this diameter, the 175 keV Mn^+ ions start to reach the back of the now thinned nanowire, the sputtering increases and the doping efficacy decreases (Figures 5.7c and 5.7d). In the evolution of the diameter with the irradiated ion fluence, plotted in Figure 5.8 as a red line, the increased sputter yield is noticeable as a slight increase in the slope of the curve at $2 \cdot 10^{17} \text{ ions/cm}^2$.

Largely because of the reduced Mn incorporation in thinned nanowires, the simulation fails to reproduce the measured Mn/Zn ratio for ion fluences of $1 \cdot 10^{17} \text{ ions/cm}^2$ and above, underestimating the Mn concentration significantly. This is due to the assumption that the probability of sputtering a Mn or a Zn/O atom is determined by the average Mn concentration in the nanowire. This would only be true if the doping profile were truly homogeneous. In

5.3 Pseudo-dynamic simulation

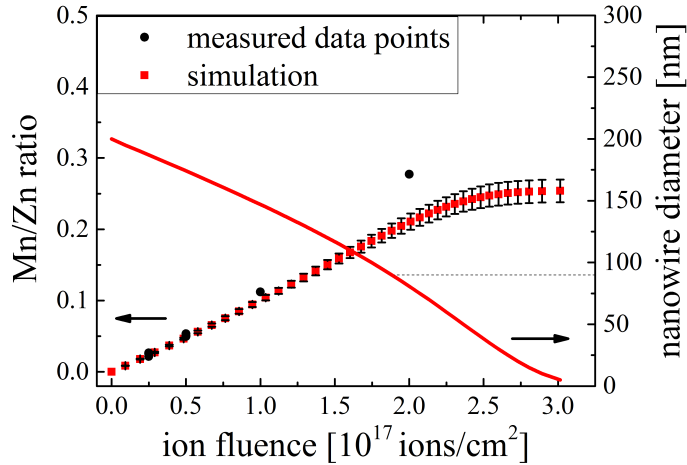


Figure 5.8: Results from a pseudo-dynamic simulation considering diameter-dependent sputtering and doping efficacy. The Mn/Zn ratio is plotted to the left axis versus the ion fluence of $175\text{ keV}Mn^+$ as red squares for the simulation and black circles for the experiment. The error bars range from the Mn/Zn ratio for 170 keV to $180\text{ keV}Mn^+$. The red line indicates the simulated nanowire diameter.

reality there is a Mn poor surface region in the doping profile shown in Figure 5.1b. In addition, as the nanowire is thinned during the irradiation, the homogeneity of the doping profile will also suffer. A peak emerges in the middle of the nanowire as the radius becomes equal to the ion range and smaller. In summary, this means that more Zn and O atoms are sputtered from the nanowire than predicted by the Mn concentration weighted sputter yield and that the core is enriched in Mn faster than the averaged doping incorporation efficacy would suggest. When the outer Mn poor layers of the nanowire are sputtered away, the Mn/Zn ratio averaged over the whole cross-section increases, even without the additional incorporation of Mn . At this point it no longer makes sense to try to predict doping concentrations with static simulations, which cannot take into account the change in the target composition and geometry. Dynamic simulations are required.

5 High Doping Concentrations in Nanowires

5.4 Summarizing Discussion

The incorporation of dopants into nanowires was studied by investigating Mn irradiated ZnO nanowires with nano-XRF. The first, perhaps slightly obvious result is that the doping concentration can be significantly influenced by shadowing of the nanowires amongst themselves. This sets some limits on the suitability of samples for homogeneous irradiation. The dense and disordered samples investigated in previous work on ion irradiated nanowires [GSM⁺08, RBGN10, KCG⁺11, Geb12, GRK⁺13, KGG⁺13, GLdR⁺14, CMCSR⁺14] for example, are very likely to show a large spread in the locally realized doping concentration. Related to this fact is the insight that control of the irradiation geometry can greatly reduce both the energy and ion fluence required to obtain a homogeneous doping concentration. The possibility of irradiation from different angles was realized in the presented case by rotation of the target. Both a reduced energy and a reduced ion fluence reduce the total damage produced in the target and can elevate the annealing requirements and thus improve the properties of doped nanowires [BMB⁺11, PKB⁺12, Bor12, KPJ⁺13, PKJ⁺14]. In any case, it was already shown that irradiated nanowires can bend in either direction relative to the ion beam, depending on the ion energy [BSL⁺11]. The rotated irradiation is a practicable alternative to complex modulations of the ion energy, which could also prevent unwanted bending of nanowires during the irradiation with high ion fluences.

The quantification of the dopants in irradiated nanowires showed that the static MC BCA code *iradina* is accurate in the prediction the doping concentration for low ion fluences. This was expected from the discussion in Chapter 2.2 on the underlying scientific background for the direct simulation of ion trajectories which translates well into nanostructures and thus naturally gives an accurate prediction of the final distribution of the ions in the target. However, because of sputtering, a reasonable upper limit to the applicability of static simulations seems to be given in these experiments by an ion fluence of $0.5 \cdot 10^{17} \text{ ions/cm}^2$. This corresponds to the reduction of the nanowires diameter by about 10%, or a reduction of the nanowire volume by roughly 20%. Note, that this result can be generalized to other target materials, ion species and

5.4 Summarizing Discussion

ion energies only if the ion range is comparable or larger than the nanowire diameter. For low ion energy irradiation, where the ion range is also low, the sputtering will effect the doped volume of the nanowire much sooner! The same holds true for other nanostructured geometries. A dynamic simulation is required once the sputtered layers amount to a sizable portion of either the implanted ion range or of the characteristic nanostructure length, which ever is smaller.

For flat target geometries, dynamic simulation tools have been available for some time [ME84, MEB88] and comparisons between simulations and experiments in studies on high fluence irradiation in thin layers and bulk targets have already observed the influence of sputtering on the doping concentration [MIS⁺91, SO93]. Unlike in nanowires, the material loss through sputtering is insignificant to the total bulk volume. However, as with the irradiation of nanostructures with low ion energies, the sputtered depth has to be compared with the ion range. When both become comparable, the interplay between sputtering and incorporation depth of dopants can lead to strong dynamics, including an oscillation of the dopant concentration along the depth of the target [Eck00].

Unfortunately, there is no straightforward way to extend the usefulness of static simulations to higher ion fluences. Although the attempted pseudo-dynamic simulations were partly able to reproduce the incorporated doping concentration or the nanowire radius, this was only possible in retrospect and by altering the simulation parameters. A predictive algorithm that is not dynamic was not found. The problem caused by the inhomogeneous incorporation of the dopant and the disproportionately large sputtering of the nanowire material can only be solved by dynamic codes, which consider both the nanostructure geometry, as well as the local concentration of each element in the target geometry. Such simulation tools are under development, if not openly available yet [Mö14].

Even in dynamic simulations, a remaining problem is posed by the sputter yield, which is not easy to simulate correctly. The case for single element materials was discussed in Chapter 4 on sputtering, but in compound or highly doped materials, the problem is significantly complicated by the possibility of

5 High Doping Concentrations in Nanowires

preferential sputtering of specific elements. In flat geometries, both the preferential sputtering of the incorporated dopant, as well as compositional changes in compounds and alloys can drastically change the final composition of the irradiated layer [Kel78, ME84, And86, MEB88, SO93, ZS95]. Due to preferential sputtering, an irradiated nanowire of a compound material may already be deficient in one of its components before a high dopant concentration is reached. At least in bulk samples the evolution of the concentration profiles for high fluence irradiations have a steady state solution. Because of mass conservation, the composition of the sputtered material is ultimately equal to the bulk material composition, which lies underneath an unstoichiometric layer effected by the irradiation [And86]. Nanowires and other nanostructures, on the other hand, are destroyed by sputtering and steady state conditions cannot arise for high fluences. The evolution of their composition for high ion fluence irradiation is therefore much less predictable.

6 Plastic Deformation of Silicon Nanowires

The experiments presented so far were conducted at temperatures high enough to ensure that the irradiated material remains crystalline. This ensures that also the density and shape of the nanowires could be preserved. The following chapter discusses the new effect of plastic deformation, which occurs in the room-temperature ion irradiation of *Si*-nanowires. Some of the experiments were performed together with Stefan Noack and are published in his Master Thesis [Noa14] and also in reference [JNW⁺15].

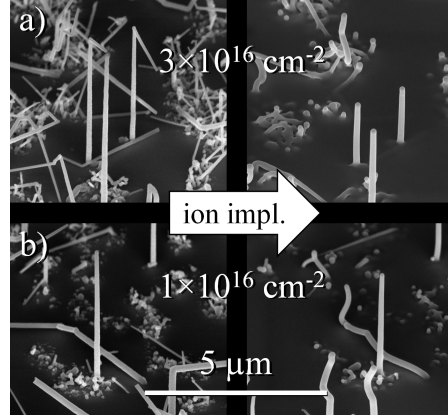
6.1 Experimental observation of plastic deformation

Silicon nanowires where irradiated at room-temperature with high ion fluences of As^+ and In^+ and/or Ga^+ with the goal of forming *Si-GaAs* or *Si-InGaAs* hetero-structures in a further annealing step [PGL⁺14, Gla15]. To characterize the process, the same individual wires were investigated after each process step, including before and after the ion irradiation. Two exemplary sets of SEM images of these samples can be seen in Figure 6.1. Clearly the nanowires shrank and widened during the ion irradiation, an effect, that has so far not been reported for ion irradiation of *Si* at such low ion energies. This is a *plastic* deformation caused by the impinging ions, because it is stable even up to high annealing temperatures [PGL⁺14, Gla15].

To investigate this deformation effect systematically, *Si*-nanowire arrays similar to the ones used for the sputtering experiment in Chapter 4.3 were

6 Plastic Deformation of Silicon Nanowires

Figure 6.1: SEM images of VLS-grown *Si*-nanowires before and after the irradiation with 90 keV In^+ and 120 keV As^+ at room temperature, while rotating the sample. The shrinking and widening of the wires is clearly visible and larger in the samples irradiated with the indicated high fluence a), than in those with a comparably low fluence b) of each ion.



irradiated with a set of Ar^+ fluences, rotating the samples under the ion beam. Argon ions were chosen for the irradiation to avoid any chemical effects, while the rotation prevented bending of the nanowires, which would have made the quantification of the deformation difficult. High-resolution SEM images were made after each irradiated ion fluence to observe and quantify the deformation. Using the algorithm described in Chapter 4.3, the profiles for the irradiated nanowires were extracted. In Figure 6.2 the black, red, green and blue lines show the diameter versus height of a single nanowire before and after irradiation with 100 keV Ar^+ up to ion fluences of 1, 3 and $5 \times 10^{16}\text{ cm}^{-2}$ respectively. In this graph, as well as in the inset black profiles, the reduction of the height by $\approx 500\text{ nm}$ and an increase of the diameter, especially at the base, can be clearly seen.

The plastic deformation does not occur during ion irradiation of crystalline *Si*-nanowires at elevated temperatures, as shown in Chapter 4.3. Only in room-temperature ion irradiation, where the *Si* amorphization threshold of 10^{14} ions/cm^2 for 100 keV Ar^+ is very low [PMB04], is the deformation observed. Nanowires first amorphized by ion irradiation and subsequently irradiated at 300°C are also deformed. Therefore, it can be concluded, that the plastic deformation under ion irradiation is an attribute of amorphous *Si*-nanowires and not of the irradiation of *Si*-nanowires at low temperatures. In crystalline *Si*-nanowires irradiated at elevated temperatures the efficient

6.2 Quantification of the Deformation

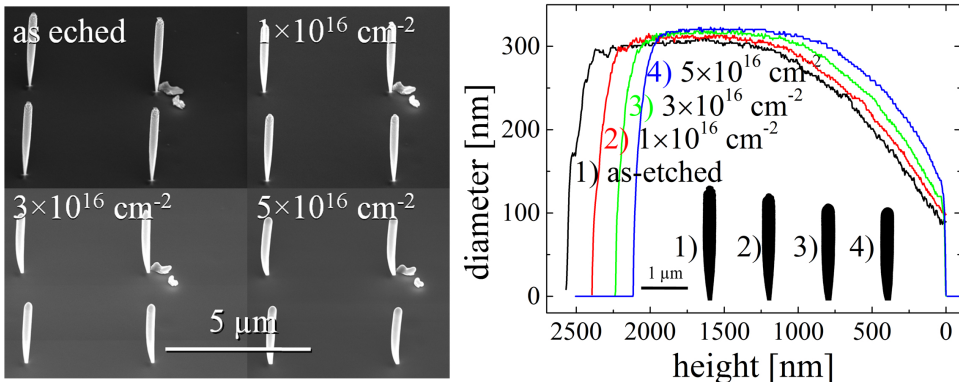


Figure 6.2: Diameter over height of a single *Si* nanowire irradiated with increasing ion fluences of 100 keV Ar^+ ions. The black insets show the profiles of the nanowire after the respective ion fluences extracted from SEM images. In both illustrations the shrinking and widening of the nanowire is clearly visible.

recombination of defects, or even recrystallization of disordered sections, reimposes the long range order of the crystal lattice onto the ion-damaged region, preventing any deformation. The amorphous nanowires, on the other hand, remain incrementally deformed after each ion impact, so that after the irradiation with a high ion fluence a large total deformation is observable.

6.2 Quantification of the Deformation

The deformation of the nanowires can be roughly quantified by simply fitting a linear trend to the ion fluence dependence of the height of the nanowires. This yields an average of 3% shrinkage per $10^{16} \text{ ions/cm}^2$. Because of outliers with larger deformation the values obtained for the 21 nanowires investigated have a large standard deviation of 3% shrinking per $10^{16} \text{ ions/cm}^2$. The tendency of the nanowires to bend during the ion irradiation made the evaluation of more nanowires impossible. This strong tendency to bend in itself indicates that the deformation process of a single ion impact is not rotationally symmetric across the cross-section of the nanowire. This comes as no surprise as the majority of impacts are off-center and thus clearly unsymmetrical. Also in Figure 6.1

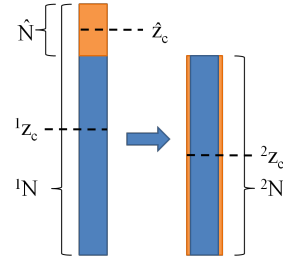
6 Plastic Deformation of Silicon Nanowires

the nanowires are clearly only imperfect cylinders as-etched. These starting inhomogeneities and especially the thinned base of the nanowires contributed to their instability during the ion irradiation.

Nevertheless, a more thorough investigation of the deformation is possible in those nanowires which remained upright, by also accounting for the height dependence of the diameter seen in Figure 6.2. On average a certain number of atoms are displaced by a certain distance along the height z of the nanowire per ion. Considering only the movement along the height z , a mass-transport rate (MTR) can be calculated according to equation 6.1:

$$\begin{aligned} MTR_{(1 \rightarrow 2)} &= [{}^1N \cdot {}^1z_c - {}^2N \cdot {}^2z_c - ({}^1N - {}^2N) \cdot {}^2z_c] / N_{ion} \\ &= {}^1N \cdot ({}^1z_c - {}^2z_c) / N_{ion} \end{aligned} \quad (6.1)$$

Figure 6.3: Illustration of the mass-transport rate calculation. Displacing 1N atoms from their average height 1z_c to the average height 2z_c requires the same mass-transport as moving \hat{N} from \hat{z}_c to 2z_c , taking into account the number of sputtered atoms ${}^1N - {}^2N$.



In equation 6.1 and Figure 6.3, ${}^{1/2}z_c$ is the height of the center of mass of the nanowire with the top left index indicating before (¹) and after (²) ion irradiation respectively. The number of atoms at height z_i can be calculated from the local radius r_i . Summing up the height weighted by the number of atoms at that height $z_c \cdot N = \sum_i \pi r_i^2 h \cdot \rho \cdot z_i$ and dividing this by the total number of atoms $N = \sum_i \pi r_i^2 h \cdot \rho$ in the nanowire gives us z_c . The sums are over all slices i of height $h = 1 \text{ pixel} = 2.7 \text{ nm}$ (typically) each. The number of ions that hit the nanowire during the irradiation of ion fluence Φ_{12} between making SEM images 1 and 2 is $N_{ion} = \sum_i ({}^1r_i + {}^2r_i) \cdot \sin(45^\circ) \cdot h \cdot \Phi_{12}$. The last term in equation 6.1 accounts for the influence of sputtered atoms. Just as in Chapter 4 on sputtering, the sputter yield could be calculated by $({}^1N - {}^2N) / N_{ion}$. Figure 6.3 illustrates two interpretations of the MTR calculation. Because only the displacement along z is considered, the direct interpretation

6.3 Knock-on transport of mass

of equation 6.1 of moving 1N atoms from their center of mass 1z_c to a new center of mass 2z_c is equivalent to moving the atoms which are ‘missing’ at the top of the nanowire after the irradiation (\hat{N} , orange volume in Figure 6.3) from their center of mass \hat{z} to 2z_c , and subtracting the sputtered atoms. This evaluation yields an average mass-transport rate of $1.2 \cdot 10^4 \text{ atoms}\cdot\text{nm}/\text{ion}$ with a standard deviation of $7 \cdot 10^3 \text{ atoms}\cdot\text{nm}/\text{ion}$. Again the large standard deviation is mainly caused by outliers with larger deformation, as can be seen in the histogram of the evaluated mass-transport rates for a couple of nanowires in Figure [?].

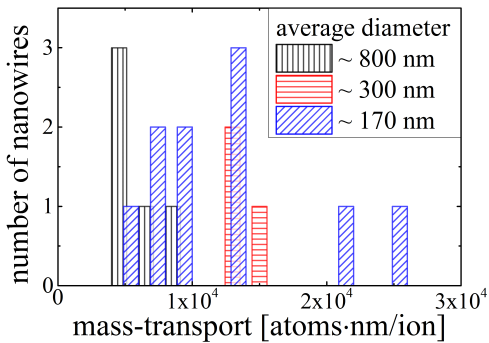


Figure 6.4: Histogram of the results of all mass-transport rates evaluated from the deformation of individual nanowires. Because of the large spread of the data points, no significant correlation between the average diameter nor the ion energy can be shown.

6.3 Knock-on transport of mass

A possible explanation for this observed plastic deformation can be sought in the linear cascade theory, which is applicable for the cascades of $100 \text{ keV } Ar^+$ in *Si*: In a collision cascade following an energetic ion impinging a solid, atoms will be preferentially ‘knocked-on’ along the propagation direction of the impinging ion. This causes an inhomogeneous distribution of interstitials and vacancies and effectively, mass is transported ‘downstream’ along the ion beam. In an amorphous material it is not clear what constitutes an ‘interstitial’ or a ‘vacancy’, but a local excess of vacancies can be understood as a locally decreased density, while an interstitial excess corresponds to an increased density. A local density gradient is not stable, because the density of amorphous *Si* before and after ion irradiation is not significantly different [PMB04]. Therefore, the density gradient introduces stress in the material,

6 Plastic Deformation of Silicon Nanowires

which can relax by plastic deformation, possibly enabled by a decreased viscosity caused by further ion irradiation [SBB97, HCA02, MAAA03, MA03].

As was shown in Chapter 4 on sputtering, BCA simulation software can accurately reproduce linear collision cascades. Therefore, a comparison between the experiments and a simulation with *iradina* can evaluate whether the deformation observed in the experiment can be accounted for by knock-on mass transport. Figure 6.5a shows the 600 nm long *Si* cylinder with a diameter of 200 nm implemented in *iradina* with $2 \times 2 \times 2\text{ nm}^3$ voxels in a simulation volume of $204 \times 204 \times 600\text{ nm}^3$. The 100 keV Ar^+ ions impinge at an angle of 45° to the z -axis. They strike the cylinder distributed uniformly along the y -direction at height $z = 0$. Figure 6.5d shows the resulting distribution of interstitials on the cross-sectional slice through the middle of the nanowire along the xz plane. This can be seen as an approximation for the distribution of the nuclear energy loss and shows the mean extent of the collision cascade. Figure 6.5e shows the same cross-section after subtracting the number of vacancies produced per ion from the number of interstitials. The excess of vacancies along the impinging plane (blue cone in the cross section) enveloped by two red planes of excess interstitials shows that there is a high probability for the ions to hit a target atom with a large impact parameter. This changes the ions path only little and displaces the target atom in a direction perpendicular to the ion beam. Superimposing many collisions along the y direction leads to the formation of one vacancy rich and two interstitial rich planes. The xy -plane in 6.5b shows the sum over the height z of the difference between interstitials and vacancies plotted to the same color scale. The illustration is dominated by vacancies at the surface of the cylinder, which are left behind by sputtered atoms.

The height distribution (summing over the radial xy plane) of the interstitials, vacancies and leaving atoms is shown in 6.5c. As expected, the majority of sputtered atoms originate near the impact height. The lines showing the interstitials and vacancies overlap in this illustration. The vacancies subtracted from the sum of interstitials and leaving atoms is plotted along the height in 6.5f. Because a displaced atom, leaving behind a vacancy, is either sputtered or becomes an interstitial, the sum over all heights of this graph is zero.

6.3 Knock-on transport of mass

The strong oscillation around $z = 0$ in 6.5f is caused by the previously discussed displacement of target atoms at an angle almost perpendicular to the ion beam for large impact parameters. This oscillation is very sensitive to the voxel-size, because, in effect, the voxel size defines a recombination length, and interstitial and vacancy rich regions are mixed in larger voxels. On the other hand, the excess of vacancies near the impact point ($\leq 70\text{ nm}$) and of interstitials further down along the ion's path ($\approx 100\text{ nm}$) is not sensitive to the voxel size. It can be used to quantify the knock-on mass transport by multiplying the plotted values by their height and integrating over all heights. The influence of the short range oscillation immediately around the impact point disappears, because here $z \approx 0$ is small. The value obtained from this calculation is $78 \pm 1 \text{ atoms}\cdot\text{nm}/\text{ion}$. Clearly this value is too low to account for the large deformation observed in the experiment where a mass-transport rate of $\geq 1 \times 10^4 \text{ atoms}\cdot\text{nm}/\text{ion}$ was assessed.

For all simulations a reasonable value for crystalline *Si*, 15 eV [CW65], was used for the displacement energy, which governs the creation of interstitials and vacancies in the simulation, as discussed in Chapter 2.2. However, in amorphous materials it is questionable what this value is supposed to mean, because point defects are not well defined. Therefore, simulations where repeated with the displacement energy set to 0 eV. As expected, the number of ‘vacancies’ and ‘interstitials’ now produced by the simulation increased dramatically. However, the long range difference between ‘vacancies’ and ‘interstitials’ seen in Figure 6.5f remains unchanged. This is an indication that the knock-on mass transport is dominated by the rare events where ions hit the target atoms directly, with low impact parameters. In these cases, a large amount of energy is transferred to the displaced atom, rendering the displacement energy irrelevant. These high energy recoils have a long trajectory, preferentially orientated in line with the ion’s momentum. On the other hand, atoms displaced with lower energies are much more numerous, but travel much shorter distances and in a randomly orientated direction. This is because most of the low energy displaced atoms are generated at the end of a branch of the collision cascade, the orientation of the branch having previously been randomized by higher energy collisions. The other low energy recoils originate

6 Plastic Deformation of Silicon Nanowires

from collisions with a high impact parameter, which leads to a large angle between the incoming particle's and the displaced particle's momentum, as seen near the impact point as a separation of interstitials and vacancies in Figure 6.5e and as the short range oscillation in Figure 6.5f. These large angle recoils also have limited energy and therefore do not contribute significantly to long range mass transport.

6.3 Knock-on transport of mass

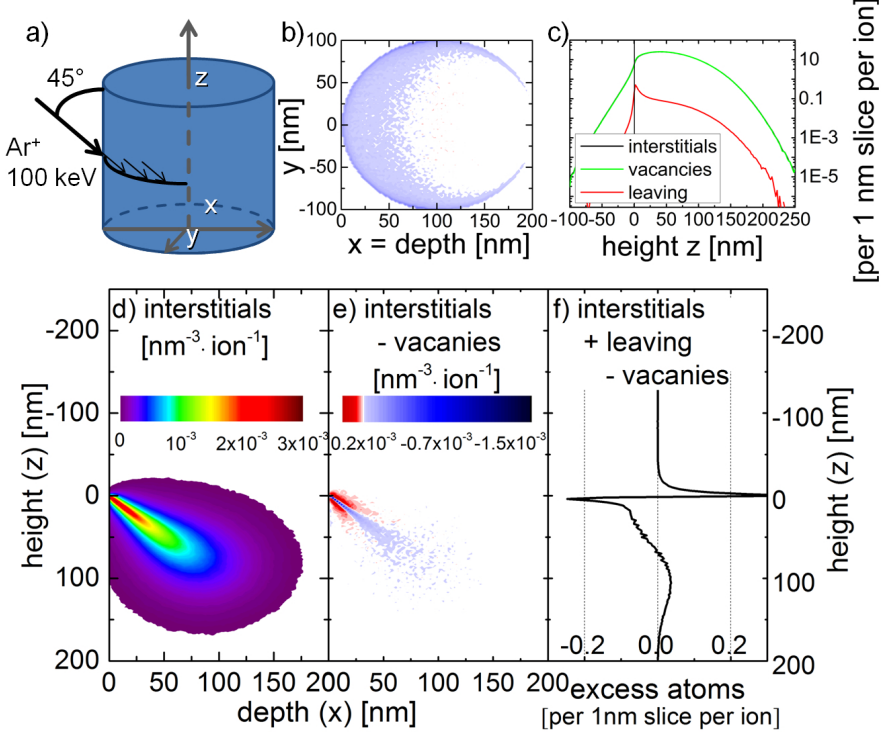


Figure 6.5: a) Illustration of the simulated irradiation geometry. All Ar^+ ions of 100 keV energy hit the nanowire volume at the same height and at an angle of 45° with respect to the nanowire axis z . The created interstitials in the radial cross-section through the middle of the simulated nanowire is shown in d). This distribution is effectively an illustration of the nuclear energy loss. In e) the vacancies are subtracted from the interstitials for the same cross-section. Summing this difference over all heights gives the radial distribution shown in b). The clear dominance of vacancies near the surface is caused by sputtering. The axial profile of the interstitials, vacancies and leaving (sputtered) atoms plotted in c) over the height relative to the impact plane shows that most atoms are sputtered at the impact height. Note that the plots of vacancies and interstitials overlap. The vacancies subtracted from the sum of interstitials and sputtered atoms plotted over the height in f) shows mass transport along the ion's path. Apart from the strong oscillation at the impact height, there is a deficiency of atoms close to the impact height ($\leq 70 \text{ nm}$) and an excess centered around 100 nm down from the impact height.

6.4 Ion irradiation at large angles of incidence

If knock-on mass-transport is not the main contribution to the deformation, the question arises whether the direction of the plastic deformation in the nanowires is related to direction of the ion beam. Will an ion irradiation from ‘below the substrate’ towards an unconstrained end of the nanowire also shrink the nanowire, or stretch it out?

Nanowires attached to a substrate are obviously not suited to answering this question, so a method to irradiate nanowires while rotating them at angles greater than 90° to the ion beam was devised. This was achieved by attaching a *Si* nanowire grown epitaxially on a *Si* wafer to an *Au* microwire, which can suspend the nanowire at arbitrary angles in the irradiation chamber. The process is shown in Figure 6.6. Platinum deposition by e-beam was used to “glue” the nanowire to the micro-manipulator in the FIB, after which the nanowire was cut from the substrate with the *Ga*-FIB. Using the *Pt*-deposition and *Ga*-FIB again, the nanowire was subsequently attached to the tip of a sharpened *Au*-microwire, which was previously glued to a piece of wafer for handling and also placed in the FIB chamber. The VLS-grown *Si* nanowires, similar to those shown in Figure 6.1, were used for this experiment, because they were readily available in longer lengths ($> 10\mu m$) than the etched nanowires.

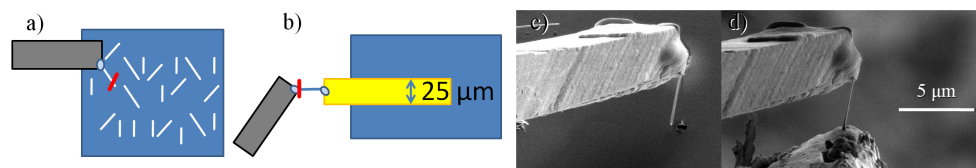


Figure 6.6: Illustration of the nanowire-on-microwire fabrication in a FIB system. The schematic a) and SEM image c) show the nanowire first glued to the micro-manipulator in the FIB by *Pt*-deposition (light blue ellipse), then cut from the substrate with the *Ga*-FIB (red line). Images b) and d) illustrate the subsequent gluing to an *Au* microwire with *Pt*-deposition and the final cut with the *Ga*-FIB to release the nanowire from the micro-manipulator.

6.5 The proposed deformation mechanism

The nanowire-on-microwire samples consisted of typically 3 – 5 nanowires, each attached to an *Au*-microwire and arranged in the irradiation chamber on a rotatable stage at an angle of 135° to the ion beam, as shown schematically in Figure 6.7a. The alignment of the nanowires to their microwire support was found to be crucial, because any shadowing of a nanowire from the ion beam on one side would lead to extreme bending of the nanowire. Only a single nanowire was found straight enough to evaluate quantitatively for more than one ion fluence irradiation step. The SEM images of this nanowire are shown in Figure 6.7b-f from a perspective perpendicular to the axis of rotation and rotated by the indicated angle around this axis. The left SEM images show the unirradiated nanowire, while the center and right images were made after the irradiation of $1 \times 10^{16} \text{ cm}^{-2}$ and $3 \times 10^{16} \text{ cm}^{-2}$ 100 keV Ar^+ , respectively. The unirradiated nanowire is straight and $3.9 \mu\text{m}$ long. The irradiated nanowire shows some bending, so the length had to be determined from a perspective where the curvature of the nanowire is in plane with the image. A fifth order polynomial was fitted to the bent shape and the length of the nanowire was thus determined to be $3.5 \mu\text{m}$ after $1 \times 10^{16} \text{ cm}^{-2}$ (6.7b) and $3.2 \mu\text{m}$ after $3 \times 10^{16} \text{ cm}^{-2}$ (6.7f). The nanowire shrank with a similar deformation rate to the previously reported 3% strain per $10^{16} \text{ ions/cm}^2$, even though the irradiation was directed towards its free end!

6.5 The proposed deformation mechanism

This experiment shows with certainty that the knock-on mass-transport is not the main contributor to the observed deformation, because it would have to be directed along the ion beam. The discussion of a possible model for the deformation will be easier by addressing similar effects and the way that simulation tools were used to understand them. The BCA MC simulation tools available inherently neglect all collective movement of atoms within the target. A field of study that has already faced the limitation of neglecting the local temperature in ion irradiation, is the irradiation with swift, heavy ions. At energies well beyond MeV, the assumption that the dominating effects will be described by binary collisions between the ion and target atoms is

6 Plastic Deformation of Silicon Nanowires

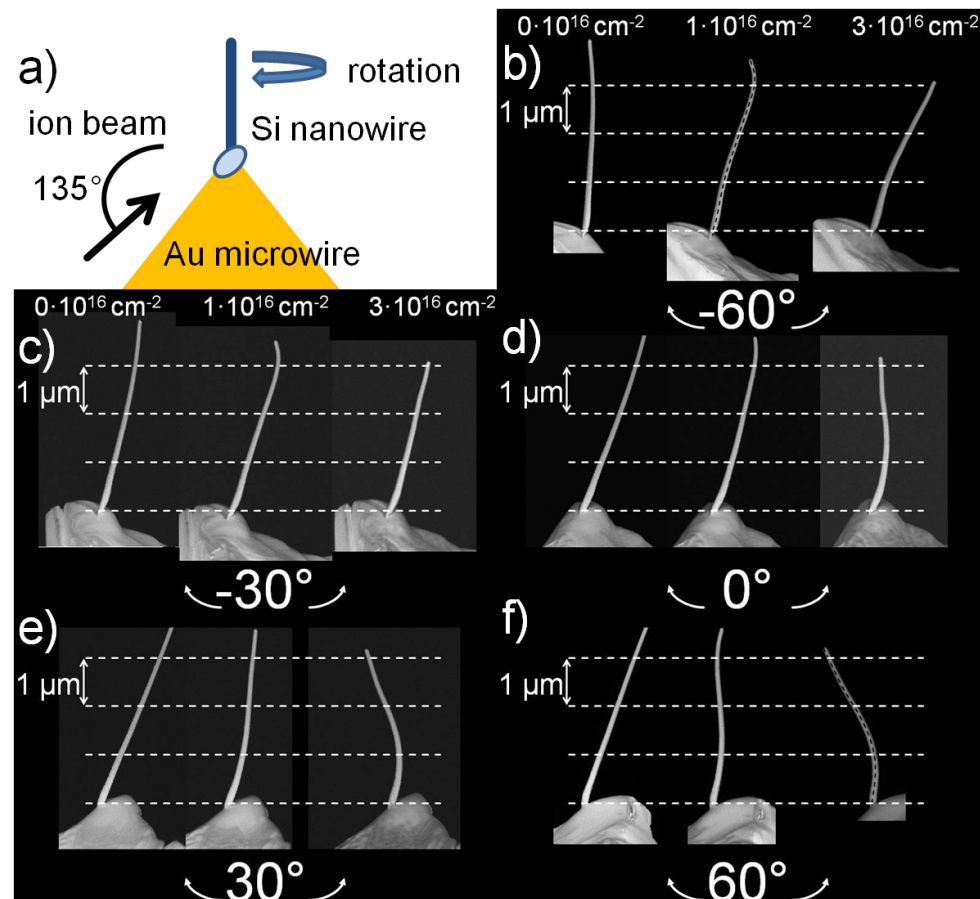


Figure 6.7: a) Illustration of the nanowire-on-microwire irradiation setup. b) - f) SEM images of the same nanowire as-mounted (left SEM images), after irradiation with $1 \times 10^{16} \text{ cm}^{-2}$ (center images), and $3 \times 10^{16} \text{ cm}^{-2}$ (right images) 100 keV Ar^+ ions. The SEM images were taken with the nanowire rotated by the indicated angle from a perspective perpendicular to the angle of rotation. The length of the nanowire after irradiation is determined in b) and f) along the dashed lines.

6.5 The proposed deformation mechanism

false. At high energies and ion masses a significant amount of energy will be transferred from the ion to the electronic system of the target. Through the relaxation mechanisms of the electronic system a part of this energy will be converted to heat in the lattice. Under certain conditions this will form “ion-tracks” in the target. One approach to understand the formation and behavior of ion-tracks is to simulate the longitudinal distribution of the deposited ion energy in the target with BCA tools (typically SRIM) and to evaluate the local temperature in a second step by following the deposited energy according to thermodynamic considerations. A good review of such “thermal spikes” can be found in reference [WKW04].

Such a thermal spike approach was successful for the description of the plastic deformation by swift heavy ion irradiation according to Trinkaus and Ryazanov [TR95] and in the understanding of material properties governing the direction of the deformation [HKW04, HKW05]. When nanoparticles are deformed [SvBvD⁺⁰⁰, SvBvD⁺⁰¹, vDSF⁺⁰¹, DPFB01, DPKB03, DDP⁺⁰⁴] an adapted version of the model by Trinkaus can be applied and the effect dubbed “ion hammering” [Kla04]. In short, according to this model the local temperature leads to a transient ‘liquid’ phase in the cylindrical volume of material around the ion’s path. Within the cylindrical geometry, the deformation by thermal expansion is anisotropic and because stresses can relax in the low-viscous volume, this is plastic deformation. As with the deformation shown in the present work, the deformation is not observed in materials that remain crystalline during the swift-heavy ion irradiation, because the long range order of the crystal lattice is reinforced upon the recrystallization during cooling. The problem with directly applying this model to the given situation is that the total energy density in the collision cascade of 100 keV Ar⁺ in Si is a low $\frac{dE}{dx} = 36 \text{ eV/nm}$, of which the electronic energy loss is roughly half. Also, the lowest ion energy for which plastic deformation of silica nanoparticles is reported is 300 keV Xe⁺ [DPKB03]. Here, the energy loss is merely $\frac{dE}{dx} = 120 \text{ eV/nm}$ with 20% lost to the electronic system. The threshold for ion tracks, however, is given at $\frac{dE}{dx} \geq 1 \text{ keV/nm}$ by Trinkaus et al. [TR95].

6 Plastic Deformation of Silicon Nanowires

The alternative to thermodynamic considerations after a MC BCA simulation are full MD simulations, where the trajectory and interaction of every atom or ion in the simulation volume is followed. This naturally includes all thermal effects, but is limited by computing power to a low number of atoms and thus a severely limited volume of material. Investigations of the self-irradiation of 10 keV Si and various metals [NGA⁺98] revealed the formation of nanoscale ‘liquid’ pockets. The term ‘liquid’ must be used with care, because it refers to a thermodynamical state of matter while the simulation timescale does not allow the assumption of thermodynamic equilibrium. Nevertheless, a sufficiently large number of atoms gain much kinetic energy (say ‘are hot’) to make the assumption effects such as a reduced viscosity and thermal expansion safe. The interesting point of this example is that the energy in the collision cascade was quite low, so that the trajectory of the initiating particle could also have been accurately simulated according to the BCA. A more recent MD investigation by Baumer et al. gets even a step closer to the presented experimental results, in that it predicts plastic deformation in metallic glasses irradiated with high energy neutrons [BD14]. The collision cascades are initiated in $a\text{-Cu}_{50}\text{Nb}_{50}$ by assuming primary knock-on atoms of 475 keV Nb . This atomistic study explicitly shows that plastic deformation caused by thermal expansion and stress relaxation can be anisotropic also in collision cascades which do not have the high energy density and symmetry required by the Trinkaus model [TR95]. Somewhat contrary results were obtained by Mayr et al. [MAAA03] where 10 eV to 100 keV recoils of Cu and Ti in $a\text{-CuTi}$ were simulated. That study comes to the conclusion that the viscous flow is dominated by ion induced point defects. It does not propose that knock-on atoms initiate the deformation, but rather, that thermal effects do not provide the main contribution to the reduced viscosity observed during ion irradiation.

The effect of anisotropic deformation within the collision cascade induced by the ion irradiation of nanowires is shown in Figure 6.8a - c. An approximately ellipsoidal volume of the target material is heated by the collision cascade. As it expands, it becomes more spherical. This anisotropic deformation is retained after cooling. The superimposition of many collision cascades

6.5 The proposed deformation mechanism

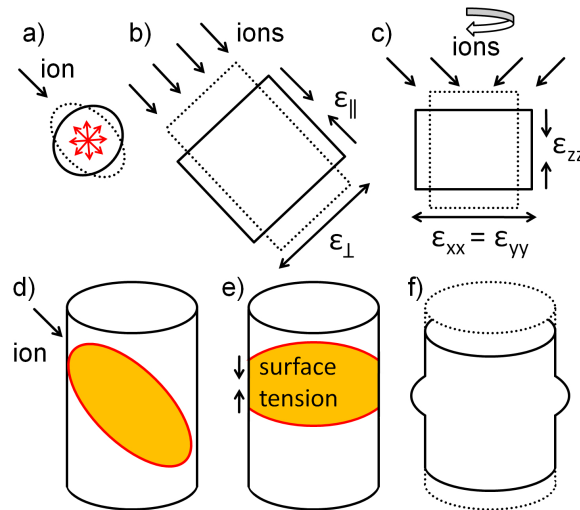


Figure 6.8: a) - c) Illustration of a deformation model analogous to ion hammering. a) The collision cascade from a single impinging ion heats an approximately ellipsoidal volume of the target material. The internal pressure will lead to an expansion towards a more spherical shape, which is retained upon cooling. b) The net effect of many ions is thus a contraction parallel to and an expansion perpendicular to the ion beam. For no change in density $\epsilon_{\parallel} = -2\epsilon_{\perp}$ has to hold. c) Under rotational symmetry this deformation translates to a contraction in the rotational axis z and an expansion in the perpendicular $x - y$ plane with $\epsilon_{zz} = -2\epsilon_{xx} = -\epsilon_{\perp}$. In d) - f) the alternative, surface tension driven deformation is illustrated. The collision-heated volume of target material shown in d). A significant slice of the nanowire shown in e) thus has a reduced viscosity. The surface energy is reduced by an increase in the local diameter of the nanowire, leading to a shortened and thickened nanowire segment shown in f).

6 Plastic Deformation of Silicon Nanowires

with a similar effect leads to a net contraction along the ion beam $\epsilon_{\parallel} < 0$ and an expansion perpendicular to it $\epsilon_{\perp} > 0$, as shown in 6.8b. To maintain constant density $-2 \cdot \epsilon_{\perp} = \epsilon_{\parallel}$. If the z -axis represents the nanowire axis, while the xy -plane is parallel to the nanowire diameter, the rotational average of this deformation around the z -axis, as illustrated in 6.8c, works out to be a contraction along this axis $\epsilon_{zz} = 1/2 \epsilon_{\parallel}$ and a corresponding expansion in the xy -plane for an angle of $\pm 45^\circ$ between the ion beam and the z -axis. Thus, the deformation rate of $d\epsilon_{zz}/d\Phi = 3\%$ strain per $10^{16} \text{ ions/cm}^2$ extracted from a linear fit to the reduction of the nanowire height requires a strain rate parallel to the ion beam of $d\epsilon_{\parallel}/d\Phi = 6\%$ strain per $10^{16} \text{ ions/cm}^2$, or $6 \cdot 10^{-18} \text{ cm}^2/\text{ion}$. This is much less than the values for the studies at higher energies reported in literature. In reference [DPKB03] a strain rate of $10^{-16} \text{ cm}^2/\text{ion}$ was reported for 300 keV Xe in silica nanoparticles and ref. [BD14] even arrives at $10^{-15} \text{ cm}^2/\text{ion}$ with MD calculations in bulk metallic glasses.

The quantitative discrepancy between the deformation observed in the experiments presented here and published studies could certainly be attributed to the lower ion energy and ion mass. One could gain confidence in this model because of the qualitative similarity to the MD simulations by Baumer et al. [BD14], which also show a deformation anisotropy within a collision cascade. However, a major difference between the MD simulation and the experiments presented here is given by the fact that in the presented experiments the collision cascade does not propagate in bulk, but in a nanostructure, where there is not much material around, and the material is not distributed around the cascade isotropically.

Therefor, a second model is presented. It relies on the surface tension as a driving force of the observed plastic deformation. In Figure 6.8d the relation between the nanowire and collision cascade is shown. Because there is not much material around, the temperature in a sizable volume of the nanowire will remain elevated for some time [Bor12, GHB⁺13, ABU15, JHMR15]. In addition, the ion irradiation itself reduces the viscosity locally [SBB97, HCA02, MAAA03], allowing the surface tension to deform the nanowire by increasing the radius locally (Figure 6.8e). The local increase in diameter and reduction in height reduces the total surface area and thus the surface energy.

6.5 The proposed deformation mechanism

In sum, the nanowire becomes shorter and wider (Figure 6.8f). Further evidence for a large influence of the surface tension during the irradiation can be found in the SEM images (Figures 6.1 and 6.2a). The nanowires look smooth and ‘molten’ after the ion irradiation, which may be an indication that they underwent a temporary, local transition into a phase of low viscosity. Also, the top facet of the nanowire is completely rounded. This smoothing and rounding of edges is not always observed in ion-irradiated nanowires, indicating that it is connected to the deformation mechanism. For example, the undeformed, crystalline *Si*-nanowires irradiated at elevated temperatures do not show such a rounded top facet (Chapter 4.3, Figure 4.4).

Thermal expansion and pressure in the volume of the nanowire heated by an ion impact may well contribute to the deformation in a similar way to the mechanism driven by the surface tension. If the heated, ellipsoidal volume intersects the nanowire surface, the pressure from the thermal expansion can vent outward, removing the force needed to drive the deformation in the other directions. Nevertheless, the outward bulging of material to the surface due to thermal expansion and pressure inside the nanowire is indistinguishable from the increasing diameter through surface tension (Figure 6.8e). The material pushed radially outward will be replaced by an axial contraction of the nanowire. Strictly speaking, this is also an anisotropic deformation, but it can be treated separately to the general, radially symmetric, but longitudinally anisotropic deformation shown in Figure 6.8a-c, because of its strong reliance on the surface. The surface tension and thermal expansion pressure drive the deformation in a nanowire in a similar way, and because both driving forces are reliant on the proximity of the surface to the collision cascade, they will be summarized as ‘surface driven’ deformation. In contrast, the general anisotropic deformation first presented is an effect contained within the collision cascade, independent of the surface.

If the plastic deformation is surface driven, it should show a strong diameter dependency, as both the surface tension itself, as well as the average ion-deposited local energy density and with it the viscosity are diameter dependent. The anisotropic deformation within a collision cascade is only diameter dependent because a limited volume of material is deformed. If the

6 Plastic Deformation of Silicon Nanowires

nanowires' diameter increases, the total volume increases, and the deformation reduces proportionally. The extremely large nanowires on the samples investigated in this thesis indeed barely show any deformation, however, this is expected for both models and thus can not be used to distinguish between the two. As stated earlier on, it was unfortunately not possible to investigate enough deformed nanowires to come up with a useful diameter dependency of the deformation.

Nevertheless, there is no inherent reason why the process of anisotropic deformation within a collision cascade should not be observable in bulk samples, yet there are no studies published on straining amorphous bulk silicon at these low ion energies. The bending of thinned *Si*-wafers would be measurable in experiments similar to those in references [Vol91, MKKP08]. The straining rate of 6% strain per $10^{16} \text{ ions/cm}^2$ in a layer of $\approx 300 \text{ nm}$, which can be predicted with from the results presented in this thesis, produces sufficient bending for said experimental method [FGN87]. It is unfortunately not clear, whether the lack of a publication of bulk deformation at low ion energies is due to the absence of the effect in bulk, or merely the absence of an experimental investigation of it. While the large interest in *Si* and ion irradiated *Si* in particular makes the latter seem somewhat unlikely, it can not be excluded.

Apart from the bulk and diameter-dependent deformation experiment already suggested, a further experiment, which could distinguish which of the two models applies, is the ion irradiation of the nanowires radially, at 90° between the nanowire axis and the ion beam. In this irradiation geometry, if the anisotropic deformation applies to each collision cascade the positive strain ϵ_\perp is now parallel to the nanowire axis. This will produce slowly elongating wires with a reduced radius. On the other hand, if the surface driven model is applicable, the nanowires will shrink regardless of the ion irradiation angle. Naturally, a similar nanowire-on-microwire setup to the one for irradiation at 135° could be used to irradiate at 90° . This experiment was undertaken, but, unfortunately, it turns out that ion irradiation at 90° is extremely prone to bending the nanowires. The bending is attributed to the *Pt* deposited used to attach the *Si* nanowire onto the *Au* microwire in the FIB fabrication of the samples. This deposition is concentrated at the base and on one side of

6.6 Summarizing Discussion

the nanowire and thus suppresses the rotational symmetry of the deformation, leading to bending. In the irradiation at 135° the base of the nanowire, where the *Pt* is deposited, is shadowed from the ion beam by the microwire, so that the nanowires are less likely to bend in this configuration. Due to the bending, the angle between the nanowire and the ion beam varied during a rotation cycle, so that a conclusive discrimination between the models can unfortunately not be made.

In conclusion, the surface tension and/or a thermal expansion directed towards the surface are the more likely driving forces for the observed plastic deformation in amorphous *Si*-nanowires than an anisotropic deformation within the collision cascade. Even though the experimental results presented do not allow a decisive proof of the deformation mechanism; due to the circumstantial evidence of the smoothed nanowires surface and the rounded nanowire tips, the surface tension is likely to provide the dominating driving force.

6.6 Summarizing Discussion

Silicon nanowires show plastic deformation when irradiated with $100\text{ keV }Ar^+$ ions at room-temperature. Using image analysis on high-resolution SEM images of ion irradiated *Si*-nanowire arrays, the ion-induced deformation rate was quantified to roughly 3% per $10^{16} ions/cm^2$ with no indication of saturation. Comparison with *iradina* simulations show that this deformation rate can not be accounted for by point defects, because the product of the number and separation between the interstitials and vacancies created in the average collision cascade is more than two orders of magnitude too low. Also, an experiment with the ion beam directed toward the unconstrained end of a suspended, rotating nanowire shows that the plastic deformation is not directed along the ion beam, but that the nanowires shrink regardless of the ion beam's alignment.

The most likely model for the plastic deformation is driven by surface tension on the surface of a small, low-viscous volume of the nanowire material near the ion impact point. This model is favored above a model driven by anisotropic deformation within the collision cascade, which shares sim-

6 Plastic Deformation of Silicon Nanowires

ilarities to the bulk deformation model developed by Trinkaus and others [TR95, BD14], because it is not clear that the proposed thermal expansion driven anisotropic deformation can transition from bulk to nanowires. The long range smoothing of the surface and rounding of edges seen in the SEM images of *Si*-nanowires irradiated at room-temperature is an additional indication that the surface tension is driving some rearrangement of material during the irradiation. This is most evident at the tips of the nanowires, which are rounded after the irradiation. Similar *Si*-nanowires irradiated at elevated temperature, which do not deform, do not show as much smoothing and maintain a flat top facet. The surface tension driven mechanism can be expected to have a strong diameter dependency, however, because of the tendency for the nanowires to bend, it was not possible to investigate enough nanowires to determine a the diameter dependency of the plastic deformation.

7 Conclusions and Outlook

The first conclusion, although it is actually almost a premise to this dissertation, is that sputtering is indeed an important effect that needs considering in high-fluence ion irradiation. This is especially true in the irradiation of nanostructures, where sputter yields can be much larger than in bulk. The diameter dependent enhancement of the sputter yield was shown for *Si*-nanowires in this thesis. These results show that a good qualitative estimation, or intuition, of how any given nanostructure will be sputtered can be obtained by using the Sigmund model for sputtering. The relative size of the overlap of the ions' nuclear energy loss and the surface of the target, even if it is nanostructured, is a reasonable estimation for the relative sputter yield. Thus, a feeling for which part of a complicated nanostructure will be most affected by sputtering during the irradiation with ions of a certain species and energy can be gained. For a specific nanoscale geometry the MC BCA simulation program *iradina* [BR11] can be used to make a more detailed analysis. The diameter dependence of the sputter yield simulated with *iradina* is qualitatively reproduced by the experiments reported in this thesis.

The quantitative values of sputtering are, in general, not accessible through the naive use of MC BCA simulations. However, very good agreement can be found for certain material and ion combinations [Bie87, HZM14], so the situation is not at all hopeless. The main difficulty is to find correct low energy interaction potential for the colliding atoms and ions for the given situation. Because the secondary ion mass spectrometry (SIMS) technique is highly reliant on sputter yields and MD simulations also require the correct interaction potential at low particle energies, there is some interest in solving this problem [ND08]. Because sputtering is dominated by low energy collisions, it is very sensitive to the interaction potential precisely at the energy range where

7 Conclusions and Outlook

it is not easily accessible to other experiments, while the available theoretical models differ. An example of interesting sputtering behavior is found in *Ni* and *Cu*, which are very similar in mass and density, yet show a factor of two difference in their sputter yield, because of differences in surface binding, electronic energy loss and nuclear interaction [Bie87].

Experiments on sputtering of defined nanostructures, such as the ones performed on nanowires within this thesis, may be a useful approach to test theoretical predictions based on different interaction potentials. This approach is not limited to semiconductor nanowires, only by the availability of the nanowires of the desired material. This is not a significant constraint, because in addition to the bottom-up growth methods, template driven nanowire synthesis methods are very versatile [Mar96]. The systematical deviation, such as the one caused in the experiments reported here by oxidation of the *Si*-nanowires can certainly be controlled by an optimized experimental protocol. Overall, a quantitative evaluation of the sputter yield should be possible. Such experiments should be combined and compared with ion impact-angle dependent measurements of the sputtering [HZM14] and the angle resolved emission of the sputtered atoms [WM08, VWMS08]. The combination of such experiments can not produce the correct interaction potential, however, it can be a powerful test for results from simulations with different interaction potentials to determine which describes the inter-atomic interaction best.

The main goal of ion irradiation is typically not sputtering, but the incorporation of dopants in the target. For nanostructured targets, care has to be taken to avoid an inhomogeneous irradiation and doping profile, which can be caused by shadowing of the ion beam in a nanostructure or amongst separate nanostructures. This was illustrated with the nano-XRF investigation of *Mn*-doped *ZnO* nanowires. The nano-XRF investigation shows that the BC MCA simulation is adequate for the prediction of the doping concentration for low ion fluences in nanowires. The limit of this applicability is given by the point where around 20% of the material affected by the ion beam is sputtered, which in nanostructures is typically 20% of the whole nanostructure's volume. Similar approximations can be made in bulk [ME84, And86, MEB88, SO93, ZS95], even if the given references don't explicitly state a limiting ion fluence or

sputtered depth. For ion irradiation with higher ion fluences, dynamic simulations are needed to predict the correct dopant concentration and profile. The limiting ion fluence can be much lower for nanostructures than in bulk, because there is less material to be sputtered and sputtering is enhanced. For high fluence ion irradiation, where more than 20% of the material is expected to be sputtered, dynamic simulations are recommended. Software, which can dynamically change the structure and composition of the ion irradiated, nanostructured target, has been revealed recently in reference [Mö14]. A comparison of the experimental results presented in this thesis with the results from such a simulation is a logical next step.

Down these lines, the application of the nano-XRF quantification technique to ion irradiated nanostructures can produce further interesting results. Because nano-XRF is highly sensitive to elemental concentrations, it can widen the scope of the proposed studies into sputtering by investigating compositional changes in ion irradiated nanostructures of compound materials. In compound materials preferential sputtering of one of the materials' components may become relevant even before a high dopant concentration has been reached. The interplay of nano-structuring, compositional changes and preferential sputtering could thus be investigated for a vast array of materials, by no means limited to semiconductors. A comparison to simulation results would further increase the understanding of the parameters influencing the preferential sputtering, which has practical meaning in secondary ion mass spectroscopy (SIMS), but also in the development of materials for fusion reactor components [Kel78, Rot90, KOW11]. Using nanowires for such an experiment has the advantage that samples with multiple diameters can be fabricated, irradiated and investigated in parallel, and thus a larger parameter space becomes accessible to simultaneous investigation.

The sputtering of nanostructures is enhanced relative to bulk, not only because of the high surface to volume ratio, but also by thermal effects. These can be very pronounced if the energy deposited by the impinging ion is confined to a small volume [GHB⁺13, IKN⁺14, NSUM14, ABU15, UBNM15]. This can lead to explosive ejection of large clusters of 1000s of atoms. Such extreme thermal sputtering effects were not observed in the experiments pre-

7 Conclusions and Outlook

sented in this thesis; firstly, because the nanowires are relatively large compared to the ion energy deposited in them, leading, on average, to only little energy deposited per atom; secondly, the ion mass and target atom mass are both relatively low, leading to a low stopping power and a low density of the energy deposition. The simulation of sputtering with the BCA and the Sigmund theory would break down in experiments where this is not the case. Nevertheless, the maximum sputter yield is observed at lower nanowire diameters in the experiment than in the simulation. This could be caused by the correlation of thermal sputtering and the number of atoms in the volume effected by the ion, because a comparable amount of energy is distributed amongst fewer atoms in thinner nanowires than in thicker ones.

That thermal effects certainly play a significant role is illustrated by the plastic deformation that *Si*-nanowires show when irradiated with medium weight Ar^+ ions at energies of 100 keV and room-temperature and not at elevated temperatures. It could be shown that this deformation is not mediated by point defects and is not directed along the ion beam. Where the lower ion energy threshold for the deformation is and whether there is an upper threshold ion energy above which the deformation ceases is not clear. The deformation is observed in amorphous *Si*-nanowires, but not in crystalline *Si*, even if both are irradiated at elevated temperatures. In the crystalline case, the efficient recrystallization of the ion damaged nanowire volume recreates the long range order of the crystal lattice after every ion impact. The amorphous material remains incrementally deformed, even if it is irradiated at elevated temperatures. This has also been observed in the plastic deformation or viscous flow of bulk samples by swift-heavy ion irradiation, which can be explained very well by ion track induced plastic deformation as proposed by Trinkaus et al. in reference [TR95]. It is clear, however, that the observed deformation in the experiments reported in this thesis is not another example of the mechanism reported by Trinkaus, because the energy loss of the ion is too low to form any sort of ion track. Also, it is not certain how the locally increased pressure required by an adaptation of this model can be confined to the limited volume of a nanowire. Therefore, a surface tension driven model, which relies on a locally reduced viscosity, was presented in this

dissertation. This model is further supported by the pronounced smoothing of the deformed nanowires' surface and edges, which is especially visible at the rounded top facet, which the crystalline, undeformed nanowires irradiated at elevated temperatures do not show.

Regardless of the underlying mechanism, the plastic deformation of *Si* has great potential for nanostructuring applications, because it is highly localized at the point of the ions impact. In combination with the relatively low ion energy required it is predestined to be used in FIB assisted fabrication of nanostructures. It may be relevant to the formation of nanopores [GTC⁺¹⁰] and certainly to the bending and manipulation of nanowires [CFL⁺¹³] and freestanding films [KCA⁺⁰⁶]. With suitable templates that may have to be thinned at the bending points, it could be possible to go as far as building '*Si*-nano-origami' similar to the metal 'origami' fabricated in reference [CCJ⁺¹³]. Such folding of *Si*-nanoshapes in particular may be a versatile fabrication tool in the growing field of *Si* MEMS devices. Furthermore, plastic deformation may have to be considered in the formulation of the mechanism for the formation of ripples on ion irradiated *Si* surfaces. The dated model by Bradley and Harper [BH88] considers only curvature and angle dependent sputtering as a roughening mechanism and is contested by models including ion induced strain and mass-transport [Nor12, KRG14]. The latter shows some similarity with the results presented here, indicating that an atomistic investigation may be necessary to resolve this issue.

All three chapters of this thesis have compared MC BCA simulations performed with *iradina* to experimental results on nanowires irradiated with high ion fluences. One limit to the applicability of the BCA is found where thermal effects have to be considered. This is not quite the case for the presented diameter-dependent sputter yields, where the simulation overlaps qualitatively with the experimental results. However, the plastic deformation found in amorphous *Si*-nanowires can not be explained with this simulation technique. Furthermore, the obtainable accuracy of *iradina* simulations of the prediction of the doping concentration in nanostructures determined with is satisfactory, but limited to low ion fluences. When the desired doping concentration is high and high ion fluences have to be implanted, dynamic simulations become

7 Conclusions and Outlook

neccessary. A rule of thumb lower limit to what constitutes a ‘high’ ion fluence is given by the fluence at which 20% of the volume effected by the ion beam is sputtered. These limitations do not formulate a criticism of the program *iradina* or the MC BCA simulation technique in general, but only serve to warn against their naive use in situations in which they are not applicable.

Bibliography

- [ABORvdBA91] Amir H. Al-Bayati, Kevin G. Orrman-Rossiter, J.A. van den Berg, and D.G. Armour. Composition and structure of the native Si oxide by high depth resolution medium energy ion scattering. *Surface Science*, 241(1-2):91–102, January 1991.
- [ABU15] Christian Anders, Eduardo M. Bringa, and Herbert M. Urbassek. Sputtering of a metal nanofoam by Au ions. *Nuclear Instruments and Methods in Physics Research Section B: Beam Interactions with Materials and Atoms*, 342:234–239, January 2015. 00000.
- [Adv15a] Advanced Functional Materials. [http://onlinelibrary.wiley.com/journal/10.1002/\(ISSN\)1616-3028](http://onlinelibrary.wiley.com/journal/10.1002/(ISSN)1616-3028). June 2015.
- [Adv15b] Advanced Materials. <http://www.advmat.de/>. June 2015.
- [And86] Hans Henrik Andersen. Computer simulations of atomic collisions in solids with special emphasis on sputtering. *Nuclear Instruments and Methods in Physics Research Section B: Beam Interactions with Materials and Atoms*, 18(1-6):321–343, January 1986.
- [ANNK02] Karsten Albe, Kai Nordlund, Janne Nord, and Antti Kuronen. Modeling of compound semiconductors: Analytical bond-order potential for Ga, As, and GaAs. *Physical Review B*, 66(3):035205, July 2002.
- [ASS69] Hh Andersen, H. Simonsen, and H. Sorensen. An Experimental Investigation of Charge-Dependent Deviations

Bibliography

- from Bethe Stopping Power Formula. *Nuclear Physics A*, A125(1):171–&, 1969. WOS:A1969C725100012.
- [AW59] B. J. Alder and T. E. Wainwright. Studies in Molecular Dynamics. I. General Method. *The Journal of Chemical Physics*, 31(2):459–466, August 1959. 01183.
- [BBF⁺88] M. N. Baibich, J. M. Broto, A. Fert, F. Nguyen Van Dau, F. Petroff, P. Etienne, G. Creuzet, A. Friederich, and J. Chazelas. Giant Magnetoresistance of (001)Fe/(001)Cr Magnetic Superlattices. *Physical Review Letters*, 61(21):2472–2475, November 1988.
- [BD14] Richard E. Baumer and Michael J. Demkowicz. Prediction of Spontaneous Plastic Deformation of Irradiated Metallic Glasses due to Thermal Spike-Induced Plasticity. *Materials Research Letters*, 2(4):221–226, October 2014.
- [Bet30] H. Bethe. Zur Theorie des Durchgangs schneller Korpuskularstrahlen durch Materie. *Annalen der Physik*, 397(3):325–400, January 1930.
- [BFS⁺12] Stuart A. Boden, Thomas M.W. Franklin, Larry Scipioni, Darren M. Bagnall, and Harvey N. Rutt. Ionoluminescence in the Helium Ion Microscope. *Microscopy and Microanalysis*, 18(06):1253–1262, December 2012.
- [BGSZ89] G. Binasch, P. Grünberg, F. Saurenbach, and W. Zinn. Enhanced magnetoresistance in layered magnetic structures with antiferromagnetic interlayer exchange. *Physical Review B*, 39(7):4828–4830, March 1989.
- [BH88] R. Mark Bradley and James M. E. Harper. Theory of ripple topography induced by ion bombardment. *Journal of Vacuum Science & Technology A*, 6(4):2390–2395, July 1988.

Bibliography

- [BHK⁺10] Thomas M. Babinec, Birgit J. M. Hausmann, Mughees Khan, Yinan Zhang, Jeronimo R. Maze, Philip R. Hemmer, and Marko Lončar. A diamond nanowire single-photon source. *Nature Nanotechnology*, 5(3):195–199, March 2010.
- [Bie87] J. P. Biersack. Computer simulations of sputtering. *Nuclear Instruments and Methods in Physics Research Section B: Beam Interactions with Materials and Atoms*, 27(1):21–36, June 1987.
- [Blo33] F. Bloch. Zur Bremsung rasch bewegter Teilchen beim Durchgang durch Materie. *Annalen der Physik*, 408(3):285–320, January 1933.
- [BMB⁺11] Christian Borschel, Maria E. Messing, Magnus T. Borgstrom, Waldomiro Paschoal, Jesper Wallentin, Sandeep Kumar, Kilian Mergenthaler, Knut Deppert, Carlo M. Canali, Hakan Pettersson, Lars Samuelson, and Carsten Ronning. A New Route toward Semiconductor Nanospintronics: Highly Mn-Doped GaAs Nanowires Realized by Ion-Implantation under Dynamic Annealing Conditions. *Nano Letters*, 11(9):3935–3940, September 2011. WOS:000294790200073.
- [BMS⁺06] C. Borchers, S. Müller, D. Stichtenoth, D. Schwen, and C. Ronning. Catalyst Nanostructure Interaction in the Growth of 1d ZnO Nanostructures. *The Journal of Physical Chemistry B*, 110(4):1656–1660, February 2006.
- [BMS⁺08] Ivan Bizyukov, Andreas Mutzke, Ralf Schneider, Alexander M. Gigler, and Karl Krieger. Morphology and changes of elemental surface composition of tungsten bombarded with carbon ions. *Nuclear Instruments and Methods in Physics Research Section B: Beam Interactions with Materials and Atoms*, 266(9):1979–1986, May 2008. 00007.

Bibliography

- [Bor12] Christian Borschel. *Ion-Solid Interaction in Semiconductor Nanowires*. PhD thesis, University Jena, Jena, 2012.
- [BR11] C. Borschel and C. Ronning. Ion beam irradiation of nanostructures – A 3d Monte Carlo simulation code. *Nuclear Instruments and Methods in Physics Research Section B: Beam Interactions with Materials and Atoms*, 269(19):2133–2138, October 2011.
- [BSL⁺11] Christian Borschel, Susann Spindler, Damiana Lerose, Arne Bochmann, Silke H. Christiansen, Sandor Nietzsche, Michael Oertel, and Carsten Ronning. Permanent bending and alignment of ZnO nanowires. *Nanotechnology*, 22(18):185307, May 2011. WOS:000288653300010.
- [BZH12] Omar Bobes, Kun Zhang, and Hans Hofsäss. Ion beam induced surface patterns due to mass redistribution and curvature-dependent sputtering. *Physical Review B*, 86(23):235414, December 2012.
- [CCJ⁺13] Khattiya Chalapat, Nikolai Chekurov, Hua Jiang, Jian Li, Babak Parviz, and G. S. Paraoanu. Self-Organized Origami Structures via Ion-Induced Plastic Strain. *Advanced Materials*, 25(1):91–95, January 2013.
- [CFL⁺13] Ajuan Cui, J. C. Fenton, Wuxia Li, Tiehan H. Shen, Zhe Liu, Qiang Luo, and Changzhi Gu. Ion-beam-induced bending of freestanding amorphous nanowires: The importance of the substrate material and charging. *Applied Physics Letters*, 102(21):213112, May 2013.
- [CMCSR⁺14] M. H. Chu, G. Martínez-Criado, J. Segura-Ruiz, S. Geburt, and C. Ronning. Nano-X-ray diffraction study of single Co-implanted ZnO nanowires: Nano-X-ray diffraction study of single NWs. *physica status solidi (a)*, 211(11):2523–2526, November 2014.

Bibliography

- [CW65] J. W. Corbett and G. D. Watkins. Production of Divacancies and Vacancies by Electron Irradiation of Silicon. *Physical Review*, 138(2A):A555–A560, April 1965.
- [CWPL01] Y. Cui, Q. Q. Wei, H. K. Park, and C. M. Lieber. Nanowire nanosensors for highly sensitive and selective detection of biological and chemical species. *Science*, 293(5533):1289–1292, August 2001. WOS:000170492600031.
- [CZC⁺10] B. Q. Cao, J. Zuniga-Perez, C. Czekalla, H. Hilmer, J. Lenzner, N. Boukos, A. Travlos, M. Lorenz, and M. Grundmann. Tuning the lateral density of ZnO nanowire arrays and its application as physical templates for radial nanowire heterostructures. *Journal of Materials Chemistry*, 20(19):3848–3854, May 2010.
- [CZP⁺12] Joseph D. Christesen, Xing Zhang, Christopher W. Pinion, Thomas A. Celano, Cory J. Flynn, and James F. Ca-hoon. Design Principles for Photovoltaic Devices Based on Si Nanowires with Axial or Radial p–n Junctions. *Nano Letters*, 12(11):6024–6029, November 2012.
- [DDP⁺04] T. van Dillen, M. J. A. de Dood, J. J. Penninkhof, A. Polman, S. Roorda, and A. M. Vredenberg. Ion beam-induced anisotropic plastic deformation of silicon microstructures. *Applied Physics Letters*, 84(18):3591–3593, May 2004.
- [Ded95] Gv Dedkov. The Interatomic Interaction Potentials in Radiation Physics. *Physica Status Solidi a-Applications and Materials Science*, 149(2):453–513, June 1995. WOS:A1995RH61400001.
- [Dha07] S. Dhara. Formation, dynamics, and characterization of nanostructures by ion beam irradiation. *Critical Reviews in Solid State and Materials Sciences*, 32(1-2):1–50, 2007. WOS:000247237500001.

Bibliography

- [DHC⁺01] X. F. Duan, Y. Huang, Y. Cui, J. F. Wang, and C. M. Lieber. Indium phosphide nanowires as building blocks for nanoscale electronic and optoelectronic devices. *Nature*, 409(6816):66–69, January 2001. WOS:000166175600038.
- [DL00] X. Duan and C. M. Lieber. General Synthesis of Compound Semiconductor Nanowires. *Advanced Materials*, 12(4):298–302, February 2000.
- [DO06] Tomasz Dietl and Hideo Ohno. Engineering magnetism in semiconductors. *Materials Today*, 9(11):18–26, November 2006.
- [DPFB01] T. van Dillen, A. Polman, W. Fukarek, and A. van Blaaderen. Energy-dependent anisotropic deformation of colloidal silica particles under MeV Au irradiation. *Applied Physics Letters*, 78(7):910–912, February 2001.
- [DPKB03] T. van Dillen, A. Polman, C. M. van Kats, and A. van Blaaderen. Ion beam-induced anisotropic plastic deformation at 300 keV. *Applied Physics Letters*, 83(21):4315–4317, November 2003.
- [Eck91] Wolfgang Eckstein. *Computer Simulation of Ion-Solid Interactions*. Springer Berlin Heidelberg, Berlin, Heidelberg, 1991.
- [Eck00] W Eckstein. Oscillations of sputtering yield. *Nuclear Instruments and Methods in Physics Research Section B: Beam Interactions with Materials and Atoms*, 171(4):435–442, December 2000.
- [EHHF92] W. Eckstein, S. Hackel, D. Heinemann, and B. Fricke. Influence of the Interaction Potential on Simulated Sputtering and Reflection Data. *Zeitschrift Fur Physik D-Atoms Molecules and Clusters*, 24(2):171–176, September 1992. WOS:A1992JQ04000013.

Bibliography

- [FGN87] Pa Flinn, Ds Gardner, and Wd Nix. Measurement and Interpretation of Stress in Aluminum-Based Metallization. *Ieee Transactions on Electron Devices*, 34(3):689–699, March 1987. WOS:A1987G468400027.
- [FH13] Brent Fultz and James Howe. *Transmission Electron Microscopy and Diffractometry of Materials*. Graduate Texts in Physics. Springer Berlin Heidelberg, Berlin, Heidelberg, 2013.
- [Fur88] J. K. Furdyna. Diluted magnetic semiconductors. *Journal of Applied Physics*, 64(4):R29–R64, August 1988.
- [Geb12] Sebastian Geburt. *Lasing and ion beam doping of semiconductor nanowires*. PhD thesis, University Jena, Jena, 2012.
- [GHB⁺13] G. Greaves, J. A. Hinks, P. Busby, N. J. Mellors, A. Ilinov, A. Kuronen, K. Nordlund, and S. E. Donnelly. Enhanced Sputtering Yields from Single-Ion Impacts on Gold Nanorods. *Physical Review Letters*, 111(6):065504, August 2013. 00004.
- [Gla15] Markus Glaser. *Personal communication, Thesis in writing*. PhD thesis, TU Wien, Wien, 2015.
- [GLdR⁺14] Sebastian Geburt, Michael Lorke, Andreia L. da Rosa, Thomas Frauenheim, Robert Röder, Tobias Voss, Uwe Kaiser, Wolfram Heimbrodt, and Carsten Ronning. Intense Intrashell Luminescence of Eu-Doped Single ZnO Nanowires at Room Temperature by Implantation Created Eu–Oi Complexes. *Nano Letters*, 14(8):4523–4528, August 2014.
- [Gou09] Brian Gough, editor. *GNU Scientific Library Reference Manual - Third Edition*. Network Theory Ltd., s.l., 3rd revised edition edition edition, January 2009.

Bibliography

- [GRK⁺13] Sebastian Geburt, Robert Röder, Uwe Kaiser, Limei Chen, Manh-Hung Chu, Jaime Segura-Ruiz, Gema Martínez-Criado, Wolfram Heimbrodt, and Carsten Ronning. Intense intra-3d luminescence and waveguide properties of single Co-doped ZnO nanowires: Intense intra-3d luminescence and waveguide properties of single Co-doped ZnO nanowires. *physica status solidi (RRL) - Rapid Research Letters*, 7(10):886–889, October 2013.
- [GS28] R. Glocke and H. Schreiber. Quantitative Röntgenspektralanalyse mit Kalterregung des Spektrums. *Annalen der Physik*, 390(8):1089–1102, January 1928.
- [GSM⁺08] S. Geburt, D. Stichtenoth, S. Müller, W. Dewald, C. Ronning, J. Wang, Y. Jiao, Y. Y. Rao, S. K. Hark, and Quan Li. Rare Earth Doped Zinc Oxide Nanowires. *Journal of Nanoscience and Nanotechnology*, 8(1):244–251, January 2008.
- [GTC⁺10] H. Bola George, Yuye Tang, Xi Chen, Jiali Li, John W. Hutchinson, Jene A. Golovchenko, and Michael J. Aziz. Nanopore fabrication in amorphous Si: Viscous flow model and comparison to experiment. *Journal of Applied Physics*, 108(1):014310, July 2010.
- [Hau84] M. Hautala. Nuclear stopping in polycrystalline materials: Range distributions and Doppler-shift attenuation analysis. *Physical Review B*, 30(9):5010–5018, November 1984. 00059.
- [HCA02] Xiaoyuan Hu, David G. Cahill, and Robert S. Averback. Burrowing of Pt nanoparticles into SiO₂ during ion-beam irradiation. *Journal of Applied Physics*, 92(7):3995–4000, October 2002.
- [HFH⁺90] S. Hackel, B. Fricke, D. Heinemann, D Kolb, and L Yang. Inter-Nuclear Potential of the System Si-Si calculated with

Bibliography

- the Finite-Element-Method. *GSI Annual Report*, page 165, 1990.
- [HH12] Robert W. Hamm and Marianne E. Hamm, editors. *Industrial Accelerators and Their Applications*. World Scientific Publishing Company, Hackensack, NJ, August 2012.
- [HIK97] C. Haginoya, M. Ishibashi, and K. Koike. Nanostructure array fabrication with a size-controllable natural lithography. *Applied Physics Letters*, 71(20):2934–2936, November 1997. WOS:A1997YF67500022.
- [HKW04] A Hedler, Siegfried Ludwig Klaumünzer, and Werner Wesch. Amorphous silicon exhibits a glass transition. *Nature Materials*, 3(11):804–809, November 2004.
- [HKW05] A. Hedler, S. Klaumünzer, and W. Wesch. Boundary effects on the plastic flow of amorphous layers during high-energy heavy-ion irradiation. *Physical Review B*, 72(5):054108, August 2005.
- [HKZ⁺10] Birgit J. M. Hausmann, Mughees Khan, Yinan Zhang, Tom M. Babinec, Katie Martinick, Murray McCutcheon, Phil R. Hemmer, and Marko Loncar. Fabrication of diamond nanowires for quantum information processing applications. *Diamond and Related Materials*, 19(5-6):621–629, June 2010. WOS:000278193600059.
- [HMF⁺01] M. H. Huang, S. Mao, H. Feick, H. Q. Yan, Y. Y. Wu, H. Kind, E. Weber, R. Russo, and P. D. Yang. Room-temperature ultraviolet nanowire nanolasers. *Science*, 292(5523):1897–1899, June 2001. WOS:000169200700044.
- [HZM14] H. Hofssäss, K. Zhang, and A. Mutzke. Simulation of ion beam sputtering with SDTrimSP, TRIDYN and SRIM. *Applied Surface Science*, 310:134–141, August 2014.

Bibliography

- [IKN⁺14] A. Ilinov, A. Kuronen, K. Nordlund, G. Greaves, J. A. Hinks, P. Busby, N. J. Mellors, and S. E. Donnelly. Sputtering yields exceeding 1000 by 80 keV Xe irradiation of Au nanorods. *Nuclear Instruments and Methods in Physics Research Section B: Beam Interactions with Materials and Atoms*, 341:17–21, December 2014.
- [JHMR15] Andreas Johannes, Henry Holland-Moritz, and Carsten Ronning. Ion beam irradiation of nanostructures: sputtering, dopant incorporation, and dynamic annealing. *Semiconductor Science and Technology*, 30(3):033001, March 2015.
- [JNGR11] Andreas Johannes, Raphael Niepelt, Martin Gnauck, and Carsten Ronning. Persistent ion beam induced conductivity in zinc oxide nanowires. *Applied Physics Letters*, 99(25):252105, 2011.
- [JNP⁺14] A. Johannes, S. Noack, W. Paschoal, S. Kumar, D. Jacobsson, H. Pettersson, L. Samuelson, K. A. Dick, G. Martinez-Criado, M. Burghammer, and C. Ronning. Enhanced sputtering and incorporation of Mn in implanted GaAs and ZnO nanowires. *Journal of Physics D-Applied Physics*, 47(39):394003, October 2014. WOS:000341772000005.
- [JNW⁺15] Andreas Johannes, Stefan Noack, Werner Wesch, Markus Glaser, Alois Lugstein, and Carsten Ronning. Anomalous Plastic Deformation and Sputtering of Ion Irradiated Silicon Nanowires. *Nano Letters*, May 2015.
- [Jon24] J. E. Jones. On the Determination of Molecular Fields. II. From the Equation of State of a Gas. *Proceedings of the Royal Society of London A: Mathematical, Physical and Engineering Sciences*, 106(738):463–477, October 1924.
- [JS82] W. Jansen and M. Slaughter. Elemental Mapping of Minerals by Electron Micro-Probe. *American Mineralogist*, 67(5-6):521–533, 1982. WOS:A1982NZ59500008.

Bibliography

- [KCA⁺06] Y.-R. Kim, P. Chen, M. J. Aziz, D. Branton, and J. J. Vlassak. Focused ion beam induced deflections of freestanding thin films. *Journal of Applied Physics*, 100(10):104322, November 2006.
- [KCG⁺11] Uwe Kaiser, Limei Chen, Sebastian Geburt, Carsten Ronning, and Wolfram Heimbrodt. Defect induced changes on the excitation transfer dynamics in ZnS/Mn nanowires. *Nanoscale Research Letters*, 6(1):228, March 2011.
- [Kel78] Roger Kelly. An attempt to understand preferential sputtering. *Nuclear Instruments and Methods*, 149(1–3):553–558, March 1978.
- [KFM⁺01] Christine Kranz, Gernot Friedbacher, Boris Mizaikoff, Alois Lugstein, Jürgen Smoliner, and Emmerich Bertagnolli. Integrating an Ultramicroelectrode in an AFM Cantilever, Combined Technology for Enhanced Information. *Analytical Chemistry*, 73(11):2491–2500, June 2001.
- [KGG⁺13] Uwe Kaiser, Sebastian Gies, Sebastian Geburt, Franziska Riedel, Carsten Ronning, and Wolfram Heimbrodt. Luminescence and energy transfer processes in ensembles and single Mn or Tb doped ZnS nanowires. *Journal of Applied Physics*, 113(7):073506, February 2013.
- [Kik28] Seishi Kikuchi. Diffraction of Cathode Rays by Mica. *Proceedings of the Imperial Academy*, 4(6):271–274, 1928.
- [Kla04] S. Klaumünzer. Ion hammering of silica colloids. *Nuclear Instruments and Methods in Physics Research Section B: Beam Interactions with Materials and Atoms*, 215(3–4):345–352, February 2004.
- [Kol12] Kurt W Kolasinski. *Surface science: foundations of catalysis and nanoscience*. Wiley, Chichester, West Sussex, United Kingdom, 2012.

Bibliography

- [KOW11] T. Kenmotsu, T. Ono, and M. Wada. Effect of deuterium retention upon sputtering yield of tungsten by deuterons. *Journal of Nuclear Materials*, 415(1, Supplement):S108–S111, August 2011.
- [KPJ⁺13] Sandeep Kumar, Waldomiro Paschoal, Andreas Johannes, Daniel Jacobsson, Christian Borschel, Anna Pertsova, Chih-Han Wang, Maw-Kuen Wu, Carlo M. Canali, Carsten Ronning, Lars Samuelson, and Håkan Pettersson. Magnetic Polarons and Large Negative Magnetoresistance in GaAs Nanowires Implanted with Mn Ions. *Nano Letters*, 13(11):5079–5084, 2013.
- [KRG14] Detlef Kramczynski, Bernhard Reuscher, and Hubert Gnaser. Wavelength-dependent ripple propagation on ion-irradiated prepatterned surfaces driven by viscous flow corroborates two-field continuum model. *Physical Review B*, 89(20):205422, May 2014.
- [KTK⁺08] Thomas J. Kempa, Bozhi Tian, Dong Rip Kim, Jinsong Hu, Xiaolin Zheng, and Charles M. Lieber. Single and Tandem Axial *p-i-n* Nanowire Photovoltaic Devices. *Nano Letters*, 8(10):3456–3460, October 2008.
- [KZB⁺09] A. Klimmer, P. Ziemann, J. Biskupek, U. Kaiser, and M. Flesch. Size-dependent effect of ion bombardment on Au nanoparticles on top of various substrates: Thermodynamically dominated capillary forces versus sputtering. *Physical Review B*, 79(15), April 2009.
- [Lin54] J. Lindhard. On the Properties of a Gas of Charged Particles. *Matematisk-Fysiske Meddelelser Kongelige Danske Videnskabernes Selskab*, 28(8):1–57, 1954. WOS:A1954XZ29300001.
- [LSH⁺08] A. Lugstein, M. Steinmair, Y. J. Hyun, G. Hauer, P. Pongratz, and E. Bertagnolli. Pressure-induced orientation con-

Bibliography

- trol of the growth of epitaxial silicon nanowires. *Nano Letters*, 8(8):2310–2314, August 2008. WOS:000258440700034.
- [Luk72] F. Lukeš. Oxidation of Si and GaAs in air at room temperature. *Surface Science*, 30(1):91–100, March 1972.
- [LW07] Charles M. Lieber and Zhong Lin Wang. Functional nanowires. *Mrs Bulletin*, 32(2):99–108, February 2007. WOS:000244600800011.
- [Mü09] Sven Müller. *Structural and optical impact of transition metal implantation into zinc oxide single crystals and nanowires*. PhD thesis, Georg-August Universität Göttingen, Göttingen, 2009.
- [Mö14] Wolfhard Möller. TRI3dyn – Collisional computer simulation of the dynamic evolution of 3-dimensional nanostructures under ion irradiation. *Nuclear Instruments and Methods in Physics Research Section B: Beam Interactions with Materials and Atoms*, 322:23–33, March 2014. 00001.
- [MA03] S. G. Mayr and R. S. Averback. Effect of ion bombardment on stress in thin metal films. *Physical Review B*, 68(21):214105, December 2003.
- [MAAA03] S. G. Mayr, Y. Ashkenazy, K. Albe, and R. S. Averback. Mechanisms of Radiation-Induced Viscous Flow: Role of Point Defects. *Physical Review Letters*, 90(5):055505, February 2003.
- [map15] ITRS road map. <http://www.itrs.net/>. April 2015.
- [Mar96] C. R. Martin. Membrane-based synthesis of nanomaterials. *Chemistry of Materials*, 8(8):1739–1746, August 1996. WOS:A1996VC73200021.
- [ME84] W. Möller and W. Eckstein. Tridyn — A TRIM simulation code including dynamic composition changes. *Nuclear*

Bibliography

- Instruments and Methods in Physics Research Section B: Beam Interactions with Materials and Atoms*, 2(1–3):814–818, March 1984.
- [MEB88] W. Möller, W. Eckstein, and J. P. Biersack. Tridyn-binary collision simulation of atomic collisions and dynamic composition changes in solids. *Computer Physics Communications*, 51(3):355–368, November 1988. 00441.
- [MIS⁺91] Y. Miyagawa, M. Ikeyama, K. Saito, G. Massouras, and S. Miyagawa. Computer simulation of dose effects on composition profiles under ion implantation. *Journal of Applied Physics*, 70(12):7289, 1991.
- [MK97] Antonio Miotello and Roger Kelly. Revisiting the thermal-spike concept in ion-surface interactions. *Nuclear Instruments and Methods in Physics Research Section B: Beam Interactions with Materials and Atoms*, 122(3):458–469, February 1997.
- [MKKP08] S. Massl, H. Köstenbauer, J. Keckes, and R. Pippan. Stress measurement in thin films with the ion beam layer removal method: Influence of experimental errors and parameters. *Thin Solid Films*, 516(23):8655–8662, October 2008.
- [MME13] Rino Micheloni, Alessia Marelli, and Kam Eshghi, editors. *Inside solid state drives (SSDs)*. Number 37 in Springer series in advanced microelectronics. Springer, Dordrecht, 2013.
- [Mol47] G. Moliere. Theorie Der Streuung Schneller Geladener Teilchen .1. *Zeitschrift Fur Naturforschung Section a-a Journal of Physical Sciences*, 2(3):133–145, 1947. WOS:A1947UW40000002.
- [MVB⁺06] J. Meijer, T. Vogel, B. Burchard, I. W. Rangelow, L. Bischoff, J. Wrachtrup, M. Domhan, F. Jelezko,

Bibliography

- W. Schnitzler, S. A. Schulz, K. Singer, and F. Schmidt-Kaler. Concept of deterministic single ion doping with sub-nm spatial resolution. *Applied Physics a-Materials Science & Processing*, 83(2):321–327, May 2006. WOS:000236641800028.
- [Nan15a] Nano Letters. <http://pubs.acs.org/journal/nalefd>. June 2015.
- [Nan15b] Nano Today. <http://journals.elsevier.com/17480132/nano-today/>. June 2015.
- [Nan15c] Nanotoxicology. <http://www.informahealthcare.com/nan>. June 2015.
- [Nas08] Nastasi/Mayer/Hirvonen. *Ion-Solid Interactions: Fundamentals and Applications*. Cambridge University Press, Cambridge ; New York, auflage: revised. edition, January 2008.
- [Nat15] Nature Nanotechnology. <http://www.nature.com/nnano>. June 2015.
- [ND08] Kai Nordlund and Sergei L. Dudarev. Interatomic potentials for simulating radiation damage effects in metals. *Comptes Rendus Physique*, 9(3–4):343–352, April 2008.
- [NGA⁺98] K. Nordlund, M. Ghaly, R. S. Averback, M. Caturla, T. Diaz de la Rubia, and J. Tarus. Defect production in collision cascades in elemental semiconductors and fcc metals. *Physical Review B*, 57(13):7556–7570, April 1998.
- [NKA⁺04] Nick S. Norberg, Kevin R. Kittilstved, James E. Ammonette, Ravi K. Kukkadapu, Dana A. Schwartz, and Daniel R. Gamelin. Synthesis of Colloidal Mn²⁺:ZnO Quantum Dots and High-TC Ferromagnetic Nanocrystalline Thin Films. *Journal of the American Chemical Society*, 126(30):9387–9398, August 2004.

Bibliography

- [Noa14] Stefan Noack. *Sputter Effects of Silicon Nanowires under Ion Bombardment*. University Jena, Master Thesis, 2014.
- [Nor95] K. Nordlund. Molecular dynamics simulation of ion ranges in the 1–100 keV energy range. *Computational Materials Science*, 3(4):448–456, March 1995. 00248.
- [Nor12] Scott Norris. Stress-induced patterns in ion-irradiated silicon: Model based on anisotropic plastic flow. *Physical Review B*, 86(23):235405, December 2012.
- [Nor14] Kai Nordlund. Correction to the Kinchin-Phase damage equation to account for athermal defect recombination and ion beam mixing: arc-dpa and rpa. In *Oral Presentation*, Leuven, September 2014.
- [NRS97] K. Nordlund, N. Runeberg, and D. Sundholm. Repulsive interatomic potentials calculated using Hartree-Fock and density-functional theory methods. *Nuclear Instruments & Methods in Physics Research Section B-Beam Interactions with Materials and Atoms*, 132(1):45–54, October 1997. WOS:A1997YF32200007.
- [NSUM14] Maureen L. Nietiadi, Luis Sandoval, Herbert M. Urbassek, and Wolfhard Möller. Sputtering of Si nanospheres. *Physical Review B*, 90(4):045417, July 2014.
- [Ogr13] Matthias Ogrisek. *Kontrolliertes Wachstum von Zinkoxid und Vanadium(IV)-oxid Nanodrähten*. University Jena, Master Thesis, 2013.
- [Ohd08] Iwao Ohdomari. Single-ion irradiation: physics, technology and applications. *Journal of Physics D: Applied Physics*, 41(4):043001, February 2008.
- [Ots79] NOBUYUKI Otsu. A Threshold Selection Method from Gray-Level Histograms. *IEEE Transactions on Systems, Man, and Cybernetics*, 9(1):62–66, 1979.

Bibliography

- [PGB13] D. Primetzhofer, D. Goebel, and P. Bauer. Local vs. non-local energy loss of low energy ions: Influence of charge exchange processes in close collisions. *Nuclear Instruments and Methods in Physics Research Section B: Beam Interactions with Materials and Atoms*, 317, Part A:8–12, December 2013.
- [PGL⁺14] Slawomir Prucnal, Markus Glaser, Alois Lugstein, Emmerich Bertagnolli, Michael Stoeger-Pollach, Shengqiang Zhou, Manfred Helm, Denis Reichel, Lars Rebohle, Marcin Turek, Jerzy Zuk, and Wolfgang Skorupa. III-V semiconductor nanocrystal formation in silicon nanowires via liquid-phase epitaxy. *Nano Research*, 7(12):1769–1776, December 2014. WOS:000346641400006.
- [PKB⁺12] Waldomiro Paschoal, Sandeep Kumar, Christian Borschel, Phillip Wu, Carlo M. Canali, Carsten Ronning, Lars Samuelson, and Hakan Pettersson. Hopping Conduction in Mn Ion-Implanted GaAs Nanowires. *Nano Letters*, 12(9):4838–4842, September 2012. WOS:000308576000069.
- [PKJ⁺14] W. Paschoal, Sandeep Kumar, D. Jacobsson, A. Johannes, V. Jain, C. M. Canali, A. Pertsova, C. Ronning, K. A. Dick, L. Samuelson, and H. Pettersson. Magnetoresistance in Mn ion-implanted GaAs:Zn nanowires. *Applied Physics Letters*, 104(15):153112, April 2014. WOS:000335145200060.
- [PMB04] Lourdes Pelaz, Luis A. Marqués, and Juan Barbolla. Ion-beam-induced amorphization and recrystallization in silicon. *Journal of Applied Physics*, 96(11):5947–5976, December 2004.
- [Pri12] D. Primetzhofer. Inelastic energy loss of medium energy H and He ions in Au and Pt: Deviations from velocity proportionality. *Physical Review B*, 86(9):094102, September 2012.

Bibliography

- [PZH⁺04] F. Patolsky, G. Zheng, O. Hayden, M. Lakadamyali, X. Zhuang, and C. M. Lieber. Electrical detection of single viruses. *Proceedings of the National Academy of Sciences*, 101(39):14017–14022, September 2004.
- [RBGN10] C. Ronning, C. Borschel, S. Geburt, and R. Niepelt. Ion beam doping of semiconductor nanowires. *Materials Science and Engineering: R: Reports*, 70(3–6):30–43, November 2010.
- [Rot90] J. Roth. Sputtering of Limiter and Divertor Materials. *Journal of Nuclear Materials*, 176:132–141, December 1990. WOS:A1990FC48200014.
- [Rut11] E Rutherford. The scattering of alpha and beta particles by matter and the structure of the atom. *Philosophical Magazine Series 6*, 21(125):669–688, May 1911.
- [SACF⁺12] Johannes Schindelin, Ignacio Arganda-Carreras, Erwin Frise, Verena Kaynig, Mark Longair, Tobias Pietzsch, Stephan Preibisch, Curtis Rueden, Stephan Saalfeld, Benjamin Schmid, Jean-Yves Tinevez, Daniel James White, Volker Hartenstein, Kevin Eliceiri, Pavel Tomancak, and Albert Cardona. Fiji: an open-source platform for biological-image analysis. *Nature Methods*, 9(7):676–682, June 2012.
- [San04] B Sankur. Survey over image thresholding techniques and quantitative performance evaluation. *Journal of Electronic Imaging*, 13(1):146, January 2004.
- [SBB53] Fm Smith, W. Birnbaum, and Wh Barkas. Measurements of Meson Masses and Related Quantities. *Physical Review*, 91(3):765–766, 1953. WOS:A1953UB46200058.
- [SBB97] E. Snoeks, K. S. Boutros, and J. Barone. Stress relaxation in tungsten films by ion irradiation. *Applied Physics Letters*, 71(2):267–269, July 1997.

Bibliography

- [Sch08] François Schiettekatte. Fast Monte Carlo for ion beam analysis simulations. *Nuclear Instruments and Methods in Physics Research Section B: Beam Interactions with Materials and Atoms*, 266(8):1880–1885, April 2008.
- [Sch12] Bernd Schmidt. *Ion beams in materials processing and analysis*. Springer, New York, 2012.
- [Sch14] Gabi Schierning. Silicon nanostructures for thermoelectric devices: A review of the current state of the art: Silicon nanostructures for thermoelectric devices. *physica status solidi (a)*, 211(6):1235–1249, June 2014.
- [SCRZ09] Guozhen Shen, Po-Chiang Chen, Koungmin Ryu, and Chongwu Zhou. Devices and chemical sensing applications of metal oxide nanowires. *J. Mater. Chem.*, 19(7):828–839, 2009.
- [Sig69] Peter Sigmund. Theory of Sputtering. I. Sputtering Yield of Amorphous and Polycrystalline Targets. *Physical Review*, 184(2):383–416, August 1969. 03204.
- [Sig73] Peter Sigmund. A mechanism of surface micro-roughening by ion bombardment. *Journal of Materials Science*, 8(11):1545–1553, November 1973.
- [Sig04] Peter Sigmund, editor. *Stopping of Heavy Ions*, volume 204 of *Springer Tracts in Modern Physics*. Springer Berlin Heidelberg, Berlin, Heidelberg, 2004.
- [Sma15] Small. <http://www.small-journal.com/>. June 2015.
- [SN06] Simon M. Sze and Kwok K. Ng. *Physics of Semiconductor Devices*. Wiley-Interscience, Hoboken, N.J, 3 edition edition, October 2006.
- [SO93] Peter Sigmund and Antonino Oliva. Alloy sputtering at high fluence: preferential sputtering and competing effects. *Nu-*

Bibliography

- clear Instruments and Methods in Physics Research Section B: Beam Interactions with Materials and Atoms*, 82(2):269–282, July 1993.
- [SPC⁺07] V. A. Solé, E. Papillon, M. Cotte, Ph. Walter, and J. Susini. A multiplatform code for the analysis of energy-dispersive X-ray fluorescence spectra. *Spectrochimica Acta Part B: Atomic Spectroscopy*, 62(1):63–68, January 2007.
- [SPTS12] Daniel Sage, D. Prodanov, J.-Y. Tinevez, and J. Schindelin. ImageJ User & Developer Conference (IUDC’12). 2012.
- [SS14] Peter Sigmund and Andreas Schinner. Notes on the Barkas-Andersen effect. *European Physical Journal D. Atomic, Molecular, Optical and Plasma Physics*, 68, 2014.
- [SSK⁺11] Janusz Sadowski, Aloyzas Siusys, Andras Kovacs, Takeshi Kasama, Rafal E. Dunin-Borkowski, Tomasz Wojciechowski, Anna Reszka, and Bogdan Kowalski. GaAs–MnAs nanowires. *physica status solidi (b)*, 248(7):1576–1580, July 2011.
- [Sti08] Daniel Stichtenoth. *Dimensionseffekte in Halbleiternanodrähten*. PhD thesis, Georg-August Universität Göttingen, Göttingen, 2008.
- [SvBvD⁺00] E. Snoeks, A. van Blaaderen, T. van Dillen, C. M. van Kats, M. L. Brongersma, and A. Polman. Colloidal Ellipsoids with Continuously Variable Shape. *Advanced Materials*, 12(20):1511–1514, October 2000.
- [SvBvD⁺01] E Snoeks, A van Blaaderen, T van Dillen, C. M van Kats, K Velikov, M. L Brongersma, and A Polman. Colloidal assemblies modified by ion irradiation. *Nuclear Instruments and Methods in Physics Research Section B: Beam Interactions with Materials and Atoms*, 178(1–4):62–68, May 2001.

Bibliography

- [SW85] Frank H. Stillinger and Thomas A. Weber. Computer simulation of local order in condensed phases of silicon. *Physical Review B*, 31(8):5262–5271, April 1985.
- [TDP92] M. Toulemonde, C. Dufour, and E. Paumier. Transient thermal process after a high-energy heavy-ion irradiation of amorphous metals and semiconductors. *Physical Review B*, 46(22):14362–14369, December 1992.
- [Ter88] J. Tersoff. New empirical approach for the structure and energy of covalent systems. *Physical Review B*, 37(12):6991–7000, April 1988.
- [Tho68] Mw Thompson. Energy Spectrum of Ejected Atoms During High Energy Sputtering of Gold. *Philosophical Magazine*, 18(152):377–&, 1968. WOS:A1968B525400015.
- [TR95] H. Trinkaus and A. I. Ryazanov. Viscoelastic Model for the Plastic Flow of Amorphous Solids under Energetic Ion Bombardment. *Physical Review Letters*, 74(25):5072–5075, June 1995.
- [UBNM15] Herbert M. Urbassek, R. Mark Bradley, Maureen L. Nettiadi, and Wolfhard Möller. Sputter yield of curved surfaces. *Physical Review B*, 91(16):165418, April 2015.
- [vDSF⁺01] T van Dillen, E Snoeks, W Fukarek, C. M van Kats, K. P Velikov, A van Blaaderen, and A Polman. Anisotropic deformation of colloidal particles under MeV ion irradiation. *Nuclear Instruments and Methods in Physics Research Section B: Beam Interactions with Materials and Atoms*, 175–177:350–356, April 2001.
- [Vol91] C. A. Volkert. Stress and plastic flow in silicon during amorphization by ion bombardment. *Journal of Applied Physics*, 70(7):3521–3527, October 1991.

Bibliography

- [VWMS08] C. Verdeil, T. Wirtz, H. N. Migeon, and H. Scherrer. Angular distribution of sputtered matter under Cs+ bombardment with oblique incidence. *Applied Surface Science*, 255(4):870–873, December 2008.
- [WDJ⁺09] Brent A. Wacaser, Kimberly A. Dick, Jonas Johansson, Magnus T. Borgström, Knut Deppert, and Lars Samuelson. Preferential Interface Nucleation: An Expansion of the VLS Growth Mechanism for Nanowires. *Advanced Materials*, 21(2):153–165, January 2009.
- [WE64] Rs Wagner and Wc Ellis. Vapor-Liquid-Solid Mechanism of Single Crystal Growth (New Method Growth Catalysis from Impurity Whisker Epitaxial + Large Crystals Si E). *Applied Physics Letters*, 4(5):89–&, 1964. WOS:A19645163A00003.
- [WHB77] W. D. Wilson, L. G. Haggmark, and J. P. Biersack. Calculations of nuclear stopping, ranges, and straggling in the low-energy region. *Physical Review B*, 15(5):2458–2468, March 1977.
- [Wie88] E Wiedemann. Über Fluorescenz und Phosphorescenz, I. Abhandlung. *Annalen der Physik*, 34:446–463, 1888.
- [WKW04] W. Wesch, A. Kamarou, and E. Wendler. Effect of high electronic energy deposition in semiconductors. *Nuclear Instruments & Methods in Physics Research Section B-Beam Interactions with Materials and Atoms*, 225(1-2):111–128, August 2004. WOS:000223792600010.
- [WM08] T. Wirtz and H. N. Migeon. Storing Matter: A new quantitative and sensitive analytical technique. *Applied Surface Science*, 255(4):1498–1500, December 2008.
- [WWS12] W. Wesch, E. Wendler, and C. S. Schnohr. Damage evolution and amorphization in semiconductors under ion irradiation. *Nuclear Instruments and Methods in Physics Research*

Bibliography

- Section B: Beam Interactions with Materials and Atoms*, 277:58–69, April 2012. 00009.
- [XYS⁺03] Y. Xia, P. Yang, Y. Sun, Y. Wu, B. Mayers, B. Gates, Y. Yin, F. Kim, and H. Yan. One-Dimensional Nanostructures: Synthesis, Characterization, and Applications. *Advanced Materials*, 15(5):353–389, March 2003.
- [YS84] Y. Yamamura and Shigeru Shindo. An empirical formula for angular dependence of sputtering yields. *Radiation Effects*, 80(1-2):57–72, January 1984.
- [Zie12] James Ziegler. *SRIM - The Stopping and Range of Ions in Matter*. February 2012.
- [ZLB85] J. F. (James F.) Ziegler, U. Littmark, and J. P. Biersack. *The stopping and range of ions in solids / J.F. Ziegler, J.P. Biersack, U. Littmark*. The Stopping and ranges of ions in matter ; v. 1. Pergamon, New York, 1985. Includes index. Bibliography: p. 308-315.
- [ZS95] Vladimir I. Zaporozchenko and Maria G. Stepanova. Preferential sputtering in binary targets. *Progress in Surface Science*, 49(2):155–196, June 1995.